

Coupling schemes for modeling hydraulic fracture propagation using the XFEM

Elizaveta Gordeliy, Anthony Peirce*

Department of Mathematics, University of British Columbia, Vancouver, British Columbia, Canada V6T 1Z2

ARTICLE INFO

Article history:

Received 9 May 2012

Received in revised form 17 August 2012

Accepted 18 August 2012

Available online 15 September 2012

Keywords:

XFEM

Hydraulic fractures

Free boundary problems

ABSTRACT

We describe coupled algorithms that use the Extended Finite Element Method (XFEM) to solve the elastic crack component of the elasto-hydrodynamic equations that govern the propagation of hydraulic fractures in an elastic medium. With appropriate enrichment, the XFEM resolves the Neumann to Dirichlet (ND) map for crack problems with $O(h^2)$ accuracy and the Dirichlet to Neumann (DN) map with $O(h)$ accuracy. For hydraulic fracture problems with a lag separating the fluid front from the fracture front, we demonstrate that the finite pressure field makes it possible to use a scheme based on the $O(h^2)$ XFEM solution to the ND map. To treat problems in which there is a coalescence of the fluid and fracture fronts, resulting in singular tip pressures, we developed a novel mixed algorithm that combines the tip width asymptotic solution with the $O(h^2)$ XFEM solution of the ND map away from the tips. Enrichment basis functions required for these singular pressure fields correspond to width power law indices $\lambda > \frac{1}{2}$, which are different from the index $\lambda = \frac{1}{2}$ of linear elastic fracture mechanics. The solutions obtained from the new coupled XFEM schemes agree extremely well with those of published reference solutions.

© 2012 Elsevier B.V. All rights reserved.

1. Introduction

Hydraulic fractures (HFs) are a class of fractures that occur in brittle materials due to the injection of a viscous fluid. HF occur both naturally and are deliberately created for engineering applications. Buoyant magma flow provides an example of a natural HF, in which magma from deep pressurized chambers is driven by buoyancy forces to propagate in finger-like fractures toward the surface of the Earth. Engineering applications include: the enhancement of the block-caving process used in mining by pre-fracturing ore bodies [1,2]; the deliberate propagation of fractures to increase the connectivity in geothermal reservoirs as well as in oil and gas reservoirs to enhance the recovery of hydrocarbons [3,4]; waste disposal; and the remediation of contaminated soils by the injection of oxidizing reagents [5,6]. There is considerable interest in developing accurate models of this complex propagation process in order to increase the design and placement of HF.

The prohibitive re-meshing cost of tracking a propagating fracture has hampered the development of domain-based methods, such as Finite Volume or Finite Element Methods [7,8], for modeling fully coupled propagating HF. The relatively recent development of the XFEM [9–11] holds much promise for the efficient numerical modeling of propagating HF within the FEM paradigm. In the XFEM methodology, the fracture is represented by enriched basis functions that are restricted to elements in the vicinity of the fracture and its tips, while field variables in the bulk of the solid medium

can be represented by standard polynomial basis functions. Thus fracture propagation can be captured even on a structured mesh by dynamically adjusting the enrichment process to incorporate the location of the moving fracture tips. Previous research on using the XFEM for HF propagation [12,13] have either focused on propagating so-called dry cracks in which the effect of fluid viscosity is not taken into account, or [14] who considered enrichment for a width field having a power law index λ within the interval $\frac{1}{2} \leq \lambda < 1$ and focused on solving the elasticity equation for both $\lambda = \frac{1}{2}$ and the viscous asymptote $\lambda = \frac{2}{3}$ [15]. However, none of this research has adequately addressed the fully-coupled HF propagation problem.

The model for HF propagation that we consider involves a degenerate PDE in the form of the Reynolds lubrication equation describing the conservation of the viscous fluid flowing within the fracture. This degenerate conservation law needs to be coupled to the equilibrium PDEs for a solid body in a state of plane strain, which express the balance of forces within the solid medium in which the fracture is propagating.

The degeneracy of the PDEs and the challenges of coupling the fluid and the solid media, each having vastly different time scales, is exacerbated by the potential for two distinct moving boundary problems – one for the fluid front and the other for the fracture front. When the fluid front and the fracture front do not coincide, in which case there is a so-called fluid lag, a zero pressure boundary condition obtains at the fluid front while the crack faces are free of pressure in the remainder of the lag region. In spite of fact that the two moving boundaries are involved, the fluid-lag problem is, in fact, simplified by the regularity of the pressure field at the fluid front and the fact that the fracture width asymptotics

* Corresponding author. Tel.: +1 604 822 2104.

E-mail address: peirce@math.ubc.ca (A. Peirce).

and fracture front location are governed by the classic square root width power law associated with Linear Elastic Fracture Mechanics (LEFM), so that the classic $\lambda = \frac{1}{2}$ enrichment basis functions can be used. However, if there is a confluence of these two fronts then the problem reduces to a single free boundary problem in which the pressure field has a singularity at the tip. This pressure singularity results in a combined front velocity that can only be determined by evaluating an indeterminate form. In addition, even though we consider a Newtonian fluid and an elastic medium, the dynamics of a propagating HF is complicated by a number of competing physical processes that are associated with length scales that can differ by several orders of magnitude. This multiscale behavior presents significant challenges for computational models of HF. Analytic and asymptotic solutions (see [16–23]), which can capture this multiscale behavior, can only be developed for the symmetric geometries for propagation in states of plane strain or radial symmetry in 3D elastic media. Thus computational models need to be developed in order to capture more complex geometries or even to incorporate simple features such as layered elastic media or material inhomogeneities. Recent developments have made it possible for numerical models [24] to achieve a high degree of accuracy with relatively few computational resources by accounting for the dominant physical process active at the computational length scale, while ignoring sub-dominant physical processes that are only important on a much finer length scale. This type of decomposition is reminiscent of matched asymptotic analysis used in boundary layer problems, in which the details at length scales finer than the computational length scale are captured by an inner asymptotic solution. This approach exploits the limiting behavior of the solution close to the crack tip, which is established by detailed asymptotic analysis [15,18,25,20].

The objective of this paper is to present two XFEM-Hydrodynamic coupling schemes, of increasing complexity, that can cope with a representative variety of tip behaviors and propagation regimes typically encountered in HF modeling. At the heart of the challenge for developing an XFEM strategy to model HF propagation is the accuracy with which it can resolve the Neumann to Dirichlet map as opposed to the Dirichlet to Neumann map. In this context the Neumann to Dirichlet map (ND) is defined as follows: given Neumann data (the fluid pressure applied to the walls of the fracture in case of a HF) the XFEM, with the appropriate tip enrichment, can be used to determine the Dirichlet data (the fracture width in the case of a HF) with an error that is $O(h^2)$ [26]. Conversely, for the Dirichlet to Neumann map the XFEM error only decreases at a rate $O(h)$. We will demonstrate that if there is a finite fluid lag, then an XFEM formulation based on inverting the ND map and using the appropriate enrichment, is sufficient to capture the HF solution with the required precision. If the fluid and fracture fronts coalesce, then the degenerate lubrication equation admits a singular pressure field, which precludes the use of a coupling scheme based on the ND map. In particular, a tip asymptotic solution, applicable at the computational length scale, is required. In order to implement this tip asymptotic solution, we have devised novel mixed scheme, which exploits both the detailed knowledge of the asymptotic solution for the fracture width in the tip and the $O(h^2)$ accuracy of the ND map to capture the solution away from the tip.

In Section 2, we describe the governing elasto-hydrodynamic equations and their non-dimensionalization. In Section 3, we describe the two XFEM formulations used in the construction of the coupled HF algorithms. In Section 4, we describe the discretization and coupling of the elasto-hydrodynamic equations as well as the iterative scheme used to locate the fluid and fracture free boundaries. In Section 5, we present the results of three numerical experiments in which we compare the XFEM solutions to published reference solutions. The first two examples involve HF propagating close to a free surface. In the first of these, the HF is initiated par-

allel to the free surface and is constrained to propagate parallel to the free surface by a high confining stress field parallel to the free surface, which resists any symmetry-breaking deviations of the crack path. In the second, the HF is initiated parallel to the free surface, but the confining stress is absent so that the crack is able to curve toward the free surface as it grows. In the third example, we consider an HF propagating in the viscosity dominated regime in an infinite elastic medium in a state of plane strain, which we compare to the so-called M-vertex solution [27,16].

2. Problem formulation

2.1. Plane strain model

Consider a hydraulic fracture growing in an impermeable elastic medium in a state of plane strain whose stiffness is characterized by the Young's modulus E and Poisson's ratio ν (see Fig. 1), and whose breaking strength is characterized by the fracture toughness K_{Ic} . The fracture is assumed to be driven by the injection of a Newtonian fluid with a dynamic viscosity μ from a point source located at the origin of the coordinate system (X, Y) , at a constant volumetric rate Q_0 per unit length in the out-of-plane direction. In two dimensions, the fracture geometry is represented by a curve $\Sigma(t)$ evolving with time t ; a curvilinear coordinate s is introduced along $\Sigma(t)$, with the origin $s = 0$ located at the fluid source. For convenient comparison with the published reference solutions, we restrict ourselves to problems in which the fracture will grow symmetrically with respect to the fluid source so that its two wings are characterized by the length $\ell(t)$ and the crack width $w(s, t)$, where $-\ell(t) < s < \ell(t)$. However, the algorithms we describe can, with little modification, be extended to non-symmetric situations. Thus the XFEM we present is in a form that can easily be generalized to model non-symmetric crack growth. Indeed, other than the front location device, which determines the time-step corresponding to a trial fracture growth increment, the implementation does not exploit the symmetry of the problem being considered. The fluid may lag behind the fracture tips, which results in two moving fluid fronts within the fracture that are located at $s = \pm \ell_f(t)$. The medium is additionally assumed to be subjected to a uniform stress state \hat{S} (such as the ambient geological confining stress field)

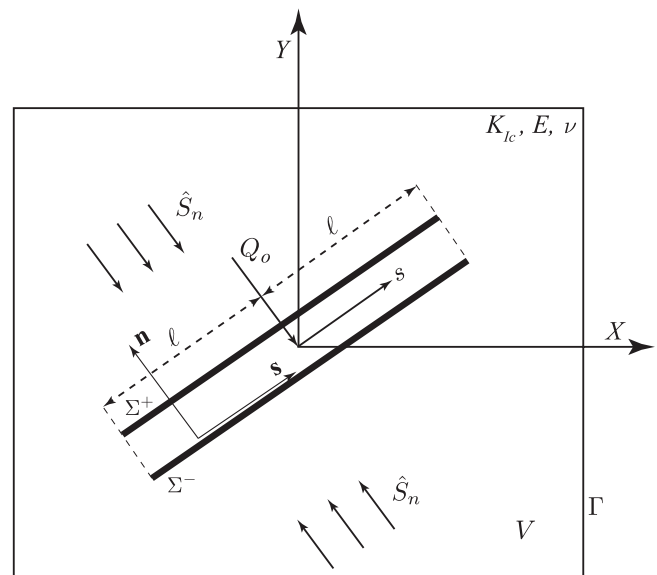


Fig. 1. This figure represents a hydraulic fracture of length 2ℓ that is assumed to grow along the curve Σ within the solid medium occupying the region V with boundary Γ due to the injection of a viscous fluid at a rate Q_0 . The fracture depicted is assumed to be subject to a normal confining stress \hat{S}_n only and no shear stress.

that can equivalently be represented by normal and shear tractions applied along the crack, denoted by $\widehat{S}_n(s)$ and $\widehat{S}_s(s)$. This stress field naturally satisfies the equilibrium equation (2) below with a zero body force vector. More general confining stress fields must also satisfy the equilibrium equation but require the inclusion of a body force field. Since we are considering a linear elastic medium it is computationally convenient to decompose the total stress field \mathbf{S}_{tot} as follows $\mathbf{S}_{tot} = \mathbf{S}_{net} + \widehat{\mathbf{S}}$. For the purposes of HF we focus on determining the net stress field \mathbf{S}_{net} knowing that the total stress field within the elastic body can be obtained by merely adding in the geological stress field $\widehat{\mathbf{S}}$. Thus by superposition, it is possible to proceed without explicitly including the body force term in the equations, provided the traction vector components $\widehat{S}_n(s)$ and $\widehat{S}_s(s)$ associated with a given body force field are known. However, for the completeness of the formulation, we will include the body force term although it will not be required for the problems considered. The solution of this moving boundary problem consists of determining: the complete fracture curve $\Sigma(t)$, the location of the fluid front $\ell_f(t)$, the fracture width $w(s, t)$, and the net pressure $p(s, t) = p_f(s, t) - \widehat{S}_n(s)$ in the fluid-filled portion of the fracture ($-\ell_f(t) < s < \ell_f(t)$), in which $p_f(s, t)$ is the fluid pressure, for a specified time t within the interval $(0, T)$.

Finally, throughout the paper it is convenient to employ scaled material parameters K' , E' and μ' , defined by

$$K' = 4 \left(\frac{2}{\pi} \right)^{1/2} K_{IC}, \quad E' = \frac{E}{1 - \nu^2}, \quad \mu' = 12\mu \quad (1)$$

2.2. Governing equations

2.2.1. Elasticity equations and corresponding boundary conditions

The displacement field \mathbf{U} and the stress field \mathbf{S} in the domain are defined with respect to the Cartesian coordinate system (X, Y) centered at the fluid source point and are represented by the components U_i and S_{ij} , respectively. The equilibrium equation for a body force field \mathbf{b} per unit volume and Hooke's law for the linear elastic medium can be written in the following tensor form

$$\nabla \cdot \mathbf{S} + \mathbf{b} = \mathbf{0} \quad (2)$$

$$\mathbf{S} = \mathbf{C} : \mathbf{E}(\mathbf{U}) \quad (3)$$

in which \mathbf{C} is the tensor of elastic constants, and $\mathbf{E}(\mathbf{U})$ is the strain tensor associated with the displacement \mathbf{U} ,

$$\mathbf{E}(\mathbf{U}) = \frac{1}{2} (\nabla \mathbf{U} + (\nabla \mathbf{U})^T) \quad (4)$$

The domain is denoted by V , while its outer boundary is denoted by Γ , and the fracture surface is denoted by Σ (see Fig. 1). At the outer boundary Γ , the displacement is assumed to be given by a known function $\mathbf{G}(X, Y)$,

$$\mathbf{U}|_{\Gamma} = \mathbf{G} \quad (5)$$

The two crack faces are identified as Σ^+ and Σ^- , and the values of the displacement and the stress along each face are denoted by \mathbf{U}^+ and \mathbf{U}^- and by \mathbf{S}^+ and \mathbf{S}^- , respectively. The unit normal and tangential vectors along the crack are denoted by \mathbf{n} and \mathbf{s} , respectively, and are oriented as shown in Fig. 1. This definition of \mathbf{n} and \mathbf{s} is consistent with the outward normal direction for the crack face Σ^- .

The normal displacement jump at a point s along the crack is equal to the crack width,

$$[[\mathbf{U}]]_{\Sigma} \cdot \mathbf{n} = (\mathbf{U}^+ - \mathbf{U}^-) \cdot \mathbf{n} = w(s, t) \quad (6)$$

The normal and shear tractions are continuous across the crack, the normal traction S_n is equal to the net pressure (but opposite in sign), and the shear traction S_s is equal to the applied shear stress, which result in the conditions:

$$S_n^+ = S_n^- = -p(s, t), \quad S_s^+ = S_s^- = \widehat{S}_s(s) \quad (7)$$

Here the superscript + or – again denotes the crack face along which the stress component is computed. The normal and the shear tractions are obtained from the stress tensor as $S_n^{\pm} = \mathbf{n}^T(\mathbf{S}^{\pm} \cdot \mathbf{n})$ and $S_s^{\pm} = \mathbf{s}^T(\mathbf{S}^{\pm} \cdot \mathbf{n})$.

2.2.2. Lubrication equation and corresponding boundary conditions

The fluid flux within the fluid-filled portion of the fracture, $q(s, t)$, is assumed to be related to the fluid pressure gradient and the fracture width via Poiseuille's law,

$$q = -\frac{w^3}{\mu'} \frac{\partial p_f}{\partial s}, \quad -\ell_f(t) < s < \ell_f(t) \quad (8)$$

and must satisfy the law of mass conservation, which is expressed by the PDE

$$\frac{\partial w}{\partial t} + \frac{\partial q}{\partial s} = Q_o \delta(s), \quad -\ell_f(t) < s < \ell_f(t) \quad (9)$$

Here $\delta(s)$ is the Dirac Delta function representing a point source at the well-bore. By combining (8) and (9), the Reynolds lubrication equation is obtained,

$$\frac{\partial w}{\partial t} = \frac{1}{\mu'} \frac{\partial}{\partial s} \left(w^3 \frac{\partial p_f}{\partial s} \right) + Q_o \delta(s), \quad -\ell_f(t) < s < \ell_f(t) \quad (10)$$

The boundary conditions for the fluid flow comprise a vanishing fluid flux at the fluid fronts, which do not necessarily coincide with the fracture fronts. The fluid-front free boundary is determined from the expression for the fluid-front velocity, which is derived from Poiseuille's law. These two conditions are expressed as follows:

$$q(\pm \ell_f(t), t) = 0 \quad (11)$$

$$\frac{d\ell_f(t)}{dt} = -\frac{w^2}{\mu'} \frac{\partial p_f}{\partial s} \quad \text{when } s = \pm \ell_f(t) \quad (12)$$

Along the fracture the net pressure field is defined to be

$$p(s, t) = \begin{cases} p_f(s, t) - \widehat{S}_n(s), & |s| < \ell_f(t) \quad \text{fluid filled region} \\ 0 - \widehat{S}_n(s), & |s| \geq \ell_f(t) \quad \text{lag region} \end{cases} \quad (13)$$

Observe that in the lag zone the fluid pressure is assumed to be zero so that the net pressure is the negative of the applied normal stress.

If there is no lag, $\ell_f(t) = \ell$ and the pressure field is typically singular at the coalescent fluid and fracture fronts. This singular pressure needs to be determined by detailed asymptotic analysis and the combined front velocity (12) needs to be evaluated using a distinguished limit. If the fracture half-length $\ell(t)$ was known, (2)–(13) would provide a closed system sufficient to determine the fracture width and the fluid pressure. An additional constraint, required for locating the moving fracture tip $\ell(t)$, is given by the propagation condition formulated in terms of the asymptotic behavior of the fracture width at the crack tips. The two limiting regimes of hydraulic fracture propagation that we consider in this paper are:

(i) the toughness dominated regime (the so-called K-vertex solution, [28,29]), is characterized by the asymptotic behavior [30]

$$w(s, t) \sim \frac{K'}{E'} \widehat{s}^{1/2}, \quad \widehat{s} \rightarrow 0 \quad (14)$$

where $\widehat{s} = (\ell \pm s)$ is the distance from the fracture tip located at $s = \mp \ell$. This regime occurs either when the fluid lag is significant so that the tip region of the fracture is not fluid-filled, or in zero lag situations in which the viscous energy dissipated by driving the fluid through the fracture is sub-dominant to the energy required to break the rock.

(ii) the viscosity dominated regime (the so-called M-vertex solution, [27,16]), is characterized by the asymptotic behavior [15]

$$w(s, t) \sim \beta_m \left(\frac{\mu'}{E'} \dot{\ell}(t) \right)^{1/3} \hat{s}^{2/3}, \quad \hat{s} \rightarrow 0 \quad \text{where } \beta_m = 2^{1/3} 3^{5/6} \quad (15)$$

This regime occurs in zero lag situations in which the energy required to break the rock is sub-dominant to the viscous energy dissipated by driving the fluid through the fracture.

By integrating the local mass balance equation (9) over the crack length and over the time since the fluid injection was initiated, and using the boundary conditions (11), we obtain the global fluid balance condition

$$\int_{-\ell_f(t)}^{\ell_f(t)} w(s, t) ds = Q_0 t \quad (16)$$

2.3. Scaling

The governing equations can be rewritten in a dimensionless form following a scaling procedure similar to that described in [31]. In order to achieve this, the following dimensionless variables are introduced,

$$t = t_* \tau, \quad X = \ell_* x, \quad Y = \ell_* y, \quad s = \ell_* \zeta, \quad \ell(t) = \ell_* \gamma(\tau), \quad \ell_f(t) = \ell_* \gamma_f(\tau) \quad (17)$$

$$w(s, t) = w_* \Omega(\zeta, \tau), \quad p(s, t) = p_* \Pi(\zeta, \tau), \quad p_f(s, t) = p_* \Pi^f(\zeta, \tau) \quad (18)$$

$$q(s, t) = Q_0 \Psi(\zeta, \tau), \quad \mathbf{b} = p_* \mathbf{f} / \ell_* \quad (19)$$

$$\mathbf{U}(X, Y) = w_* \mathbf{u}(x, y), \quad \mathbf{S}(X, Y) = p_* \boldsymbol{\sigma}(x, y), \quad \hat{S}_n = p_* \hat{\sigma}_n, \quad \hat{S}_s = p_* \hat{\sigma}_s \quad (20)$$

where t_* , ℓ_* , w_* and p_* are the characteristic scales for time, length, the crack width and the net pressure that are active in the problem. The dimensionless quantities are: the time τ , the Cartesian coordinates (x, y) , the tangential coordinate along the crack ζ , the crack half-length γ , the fluid front location γ_f , the net pressure Π , the fluid pressure Π^f , the crack width Ω , the fluid flux Ψ , the displacement \mathbf{u} , the stress $\boldsymbol{\sigma}$, and the scaled body force field \mathbf{f} .

When the governing equations are reformulated in terms of the dimensionless variables, the following four dimensionless groups can be identified in the governing equations:

$$\mathcal{G}_e = \frac{E' w_*}{p_* \ell_*}, \quad \mathcal{G}_v = \frac{Q_0 t_*}{w_* \ell_*}, \quad \mathcal{G}_m = \frac{\mu' \ell_*^2}{w_*^2 p_* t_*}, \quad \mathcal{G}_k = \frac{K' \ell_*^{1/2}}{E' w_*} \quad (21)$$

In order to reformulate the governing equations in terms of the dimensionless variables of order one, three of these groups are set to 1. These three constraints combined with a characteristic length or time scale of interest, such as the maximum fracture length expected in the simulation or the specified maximum injection time T , are used to identify the four characteristic scales t_* , ℓ_* , w_* and p_* . Proceeding in this way two distinct scalings emerge:

- Toughness scaling: $\mathcal{G}_e = \mathcal{G}_v = \mathcal{G}_k = 1$. Combining these three conditions with the definitions of the dimensionless groups (21) we obtain the following power-law relationships between the characteristic length, width, and pressure time scales:

$$\ell_* = \left(\frac{E' Q_0}{K'} \right)^{2/3} t_*^{2/3}, \quad w_* = \left(\frac{K^2 Q_0}{E'^2} \right)^{1/3} t_*^{1/3}, \quad p_* = \left(\frac{K^4}{E' Q_0} \right)^{1/3} t_*^{-1/3} \quad (22)$$

The dimensionless viscosity in this scaling $\mathcal{G}_m = \frac{\mu' E^3 Q_0}{K^4} := \mathcal{M}$ is considered a parameter.

- Viscosity scaling: $\mathcal{G}_e = \mathcal{G}_v = \mathcal{G}_m = 1$. Combining these three conditions with the definitions of the dimensionless groups (21) we obtain the following power-law relationships between the characteristic length, width, and pressure time scales:

$$\ell_* = \left(\frac{E' Q_0^3}{\mu'} \right)^{1/6} t_*^{2/3}, \quad w_* = \left(\frac{\mu' Q_0^3}{E'} \right)^{1/6} t_*^{1/3}, \quad p_* = (\mu' E^2)^{1/3} t_*^{-1/3} \quad (23)$$

The dimensionless toughness in this scaling $\mathcal{G}_k = \left(\frac{K^4}{\mu' E^3 Q_0} \right)^{1/4} := \mathcal{K} = \mathcal{M}^{-1/4}$ is considered a parameter.

The governing equations and boundary conditions can then be rewritten in the following dimensionless form:

- Equilibrium equation

$$\nabla \cdot \boldsymbol{\sigma} + \mathbf{f} = \mathbf{0} \quad (24)$$

- Hooke's law

$$\boldsymbol{\sigma} = \mathcal{C} : \boldsymbol{\varepsilon}(\mathbf{u}) \quad (25)$$

in which \mathcal{C} is the scaled elasticity tensor, $\mathcal{C} = \mathbf{C}/E'$, and $\boldsymbol{\varepsilon}(\mathbf{u})$ is the strain tensor associated with the scaled displacement \mathbf{u} and scaled coordinates (x, y) ,

$$\boldsymbol{\varepsilon}(\mathbf{u}) = \frac{1}{2} (\nabla_{x,y} \mathbf{u} + (\nabla_{x,y} \mathbf{u})^T) \quad (26)$$

- Boundary conditions for the displacement and stress field

$$\mathbf{u}|_{\Gamma} = \mathbf{g} \quad (27)$$

$$[[\mathbf{u}]]_{\Sigma} \cdot \mathbf{n} = (\mathbf{u}^+ - \mathbf{u}^-) \cdot \mathbf{n} = \Omega(\zeta, \tau) \quad (28)$$

$$\sigma_n^+ = \sigma_n^- = -\Pi(\zeta, \tau), \quad \sigma_s^+ = \sigma_s^- = \hat{\sigma}_s(\zeta) \quad (29)$$

where $\mathbf{g} = \mathbf{G}/w_*$ is the scaled prescribed displacement at the outer boundary Γ , and $\sigma_\eta^\pm = S_\eta^\pm/p_*$ for $\eta = n, s$ are the scaled normal and shear stresses;

- Poiseuille's law

$$\Psi = -\Omega^3 \frac{\partial \Pi^f}{\partial \zeta} \quad (30)$$

- Conservation law

$$\dot{\Omega} + \frac{\partial \Psi}{\partial \zeta} = \delta(\zeta) \quad (31)$$

where we use the notation $\dot{\Omega} = \frac{\partial \Omega}{\partial \tau}$;

- Boundary conditions at the fluid fronts

$$\Psi(\pm \gamma_f(\tau), \tau) = 0, \quad \dot{\gamma}_f(\tau) = -\Omega^2 \frac{\partial \Pi^f}{\partial \zeta}, \quad \zeta = \pm \gamma_f(\tau) \quad (32)$$

- Net pressure in the lag region

$$\Pi(\zeta, \tau) = -\hat{\sigma}_n(\zeta), \quad |\zeta| > \gamma_f \quad (33)$$

- Propagation conditions for the toughness or viscosity dominated cases, respectively:

$$\Omega \sim \mathcal{K} \hat{\zeta}^{1/2}, \quad \hat{\zeta} \ll 1 \quad (34)$$

$$\Omega \sim \beta_m \dot{\gamma}(\tau)^{1/3} \hat{\zeta}^{2/3}, \quad \hat{\zeta} \ll 1 \quad (35)$$

where $\hat{\zeta}$ is the distance from the crack tip and $\hat{\zeta} = \gamma \pm \zeta$ in the vicinity of the crack tips at $\zeta = \mp \gamma$, respectively.

The Reynolds lubrication equation and the global volume balance equation assume the dimensionless form

$$\dot{\Omega} = \frac{\partial}{\partial \zeta} \left(\Omega^3 \frac{\partial \Pi}{\partial \zeta} \right) + \delta(\zeta) \quad (36)$$

$$\int_{-\gamma_f}^{\gamma_f} \Omega d\zeta = \tau \quad (37)$$

3. The XFEM for elastic boundary value problems in a domain with a crack

XFEM strategies are developed in [26] to solve two types of boundary value problems that are important for modeling hydraulic fracture problems. We briefly outline these formulations. The two types of boundary conditions considered are:

(I) $P \rightarrow W$ (Neumann to Dirichlet map: ND): given a prescribed pressure $\Pi_n(\zeta)$ along Σ determine the crack opening displacement $\Omega(\zeta)$,

$$\Pi(\zeta) = \Pi_n(\zeta), \quad \zeta \in \Sigma \quad (38)$$

(II) P&W (mixed: interior Neumann to Dirichlet ND, given tip widths): given the crack opening displacement $\Omega_t(\zeta)$ in a neighborhood Σ_t of the crack tip and the prescribed pressure $\Pi_c(\zeta)$ in the interior of the crack $\Sigma_c = \Sigma \setminus \Sigma_t$, determine the crack opening displacement $\Omega(\zeta)$ along Σ_c ,

$$\Omega(\zeta) = \Omega_t(\zeta), \quad \zeta \in \Sigma_t; \quad \Pi(\zeta) = \Pi_c(\zeta), \quad \zeta \in \Sigma_c \quad (39)$$

We also consider a general class of tip asymptotic behavior in the limit as the distance ζ to the fracture tip tends to zero:

$$\Omega_t(\zeta) \stackrel{\zeta \rightarrow 0}{\sim} A \zeta^{2\lambda}, \quad \text{where } \frac{1}{2} \leq \lambda < 1 \quad (40)$$

for some constant A . It can be shown [32] by local analysis of the tip asymptotics that the corresponding pressure behavior is of the form $\Pi_t \stackrel{\zeta \rightarrow 0}{\sim} \frac{1}{4} A \lambda \cot(\pi \lambda) \zeta^{2\lambda-1}$ when $\frac{1}{2} < \lambda < 1$. Consistent with this asymptotic behavior, the appropriate enrichment basis functions for the displacement and corresponding stress fields are of the form (see [26]):

$$\psi^{\mathbf{u},\lambda} = r^\lambda \{ \sin(\lambda\theta), \cos(\lambda\theta), \sin(\lambda-2)\theta, \cos(\lambda-2)\theta \} \quad (41)$$

$$\psi^{\sigma,\lambda} = r^{\lambda-1} \{ \sin(\lambda-1)\theta, \cos(\lambda-1)\theta, \sin(\lambda-3)\theta, \cos(\lambda-3)\theta \} \quad (42)$$

where (r, θ) are polar coordinates centered at the fracture tip, so that the values $\theta = \pm\pi$ correspond to the two crack faces.

3.1. $P \rightarrow W$ scheme

3.1.1. Weak formulation

Following [33] the domain V is discretized into a finite element mesh comprising a set of non-overlapping quadrilateral elements. The displacement in V is approximated by elements of the trial space $\mathcal{U}_\Sigma^h = \{\mathbf{u}^h | \mathbf{u}^h \in U, \mathbf{u}^h = \mathbf{g} \text{ on } \Gamma\}$ while variations are taken from the test space $\mathcal{V}_\Sigma^h = \{\mathbf{v}^h | \mathbf{v}^h \in U, \mathbf{v}^h = \mathbf{0} \text{ on } \Gamma\}$. Here U is a finite-dimensional subspace of the Sobolev space $H^1(V \setminus \Sigma) \times H^1(V \setminus \Sigma)$ that consists of the shape functions representing the discretization \mathbf{u}^h . The domain $V \setminus \Sigma$ that does not contain the crack Σ is assumed to be piecewise Lipschitz. The test and trial functions are assumed to be discontinuous in a direction normal to the crack Σ .

For a test function \mathbf{u}^h that is represented by a linear combination of shape functions, the corresponding strain $\boldsymbol{\varepsilon}(\mathbf{u}^h)$ can be computed from (26), while the corresponding stress can be obtained from Hooke's law (25) to yield $\boldsymbol{\sigma}(\mathbf{u}^h) = \mathcal{C} : \boldsymbol{\varepsilon}(\mathbf{u}^h)$. The discretized formulation of the elasticity problem (24)–(29) and (38) seeks to find $\mathbf{u}^h \in \mathcal{U}_\Sigma^h$ such that

$$\begin{aligned} 0 &= \int_{V \setminus \Sigma} \boldsymbol{\varepsilon}(\mathbf{v}^h) \\ &: \boldsymbol{\sigma}(\mathbf{u}^h) dV - \int_{V \setminus \Sigma} \mathbf{v}^h \cdot \mathbf{f} dV + \int_{\Sigma} [[\mathbf{v}^h]] \cdot (-\Pi_n(\zeta) \mathbf{n} + \tilde{\sigma}_s(\zeta) \mathbf{s}) d\zeta \end{aligned} \quad (43)$$

for all $\mathbf{v}^h \in \mathcal{V}_\Sigma^h$. In the above, $[[\mathbf{v}]] = (\mathbf{v}^+ - \mathbf{v}^-)$ denotes the jump of \mathbf{v} across the crack.

3.1.2. Shape functions with fixed radius enrichment

Following [33] the crack is represented by two forms of enrichment, namely: Heaviside enrichment ($H(\mathbf{x}) = (\pm 1)$ if $\mathbf{x} \in \Sigma^\pm$ and $H(\mathbf{x}) = 0$ if \mathbf{x} is on the crack) used to define the crack geometry, and tip enrichment, given by the four singular functions $\{\psi_j^{\mathbf{u}}\}$ defined in (41), that is used to represent the singular behavior at the fracture tips. The tip enrichment is introduced at all nodes that are within a prescribed radius ρ from the crack tip \mathbf{x}_{tip} , i.e., $I_t = \{i \in I : |\mathbf{x}_i - \mathbf{x}_{tip}| \leq \rho\}$, where $\mathbf{x}_i \in V$ denote coordinates of the finite element node i , and I is the set of all nodes. Heaviside enrichment is introduced for nodes of the set I_H comprising all the nodes of the elements cut by the crack, excluding the nodes already in I_t , so that $I_t \cap I_H = \emptyset$.

The finite-dimensional Galerkin space U is defined by $U = H^{1h} \times H^{1h}$ and is spanned by the following shape functions:

$$\begin{aligned} H^{1h} &= \left\{ \sum_{i \in I} a_i N_i(\mathbf{x}) + R_H(\mathbf{x}) \sum_{i \in I_H} b_i N_i(\mathbf{x}) (H(\mathbf{x}) - H(\mathbf{x}_i)) \right. \\ &\quad \left. + R_t(\mathbf{x}) \sum_{i \in I_t} N_i(\mathbf{x}) \sum_{j=1}^4 c_j^i (\psi_j^{\mathbf{u}}(\mathbf{x}) - \psi_j^{\mathbf{u}}(\mathbf{x}_i)) \right\} \end{aligned} \quad (44)$$

where $\mathbf{x} \in V \setminus \Sigma$; N_i are the standard piecewise linear Lagrange basis functions; and $a_i, b_i, c_j^i \in \mathbb{R}$. Here I_H^* is the set of nodes enriched by the Heaviside function and all nodes in elements that are cut by the crack and which have Heaviside-enriched nodes, and I_t^* is the set of tip-enriched nodes and all nodes in elements that have tip-enriched nodes. In addition, the two blending functions $R_t(\mathbf{x}) = \sum_{i \in I_t} N_i(\mathbf{x})$ and $R_H(\mathbf{x}) = 1 - R_t(\mathbf{x})$ are introduced to blend the two enrichments (see [33,34]) so that the representation (44) maintains the partition of unity property [35] that is sufficient to obtain an optimal convergence rate for the XFEM [36].

3.2. P&W scheme

3.2.1. Weak formulation

We use the localized mixed hybrid formulation introduced by Zilian and Fries [37] to specify the displacement jump Ω_t along that part of the domain which is adjacent to the crack boundary Σ_t , and use an approach similar to the formulation in the $P \rightarrow W$ scheme for the rest of the domain. The domain V is discretized into a mesh \mathcal{M} of non-overlapping quadrilateral elements e each of which occupies the region V_e^h having an elemental boundary ∂V_e^h , such that: $V = \cup_{e \in \mathcal{M}} V_e^h$. The subset of elements that overlap with that part of the crack Σ_t along which Ω_t is prescribed is denoted \mathcal{K} : $\mathcal{K} = \{e \in \mathcal{M} : V_e^h \cap \Sigma_t \neq \emptyset\}$. The domain V is thus artificially partitioned into two domains: V_o and $\cup_{e \in \mathcal{K}} V_e^h$, where $V_o = V \setminus \cup_{e \in \mathcal{K}} V_e^h$ contains all elements that do not overlap with Σ_t .

To approximate the displacement in V , we use the same test and trial function spaces \mathcal{U}_Σ^h and \mathcal{V}_Σ^h that were introduced for the $P \rightarrow W$ scheme, with the shape functions in $U = H^{1h} \times H^{1h}$. However, in each element $e \in \mathcal{K}$, the stress $\boldsymbol{\sigma}$ is introduced as an auxiliary tensor variable for which Hooke's law (25) is weakly imposed. Following [37] we approximate $\boldsymbol{\sigma}$, by introducing the test (and trial) tensor function space

$$\mathcal{S}_\sigma^h = \{\boldsymbol{\sigma}^h | \sigma_{ij}^h = \sigma_{ji}^h, \sigma_{ij}^h \in H^{-1h} \text{ for } i, 2 \text{ and } j = 1, 2\}$$

in which H^{-1h} is a finite-dimensional subspace of the space of functions that are square-integrable in each element in \mathcal{K} and which are discontinuous at the element edges and in a direction normal to the crack Σ . In the next subsection we define the shape functions for this subspace on the element level for each $e \in \mathcal{K}$.

The discretized formulation of the elasticity problem (24)–(29) and (39) seeks to find $(\mathbf{u}^h, \boldsymbol{\sigma}^h) \in \mathcal{U}_u^h \times \mathcal{S}_\sigma^h$ such that, for all $(\mathbf{v}^h, \boldsymbol{\tau}^h) \in \mathcal{V}_u^h \times \mathcal{S}_\sigma^h$,

$$0 = \int_{V_0 \setminus \Sigma} \boldsymbol{\varepsilon}(\mathbf{v}^h) : \boldsymbol{\sigma}(\mathbf{u}^h) dV - \int_{V_1 \setminus \Sigma} \mathbf{v}^h \cdot \mathbf{f} dV + \int_{\Sigma_c} [[\mathbf{v}^h]] \cdot (-\Pi_c(\zeta) \mathbf{n} + \hat{\sigma}_s(\zeta) \mathbf{s}) d\zeta \quad (45)$$

$$+ \sum_{e \in \mathcal{K}} \int_{V_e^h \setminus \Sigma} \boldsymbol{\varepsilon}(\mathbf{v}^h) : \boldsymbol{\sigma}^h dV + \sum_{e \in \mathcal{K}} \int_{V_e^h \setminus \Sigma} \boldsymbol{\tau}^h : (\boldsymbol{\varepsilon}(\mathbf{u}^h) - \mathcal{C}^{-1} : \boldsymbol{\sigma}^h) dV \quad (46)$$

$$+ \sum_{e \in \mathcal{K}} \int_{\Sigma_{t,e}} ([[\mathbf{v}^h]] \cdot \mathbf{n})(\mathbf{n} \cdot \{\boldsymbol{\sigma}^h\} \cdot \mathbf{n}) + (\mathbf{n} \cdot \{\boldsymbol{\tau}^h\} \cdot \mathbf{n})([[\mathbf{u}^h]] \cdot \mathbf{n} - \Omega_t(\zeta)) + ([[\mathbf{v}^h]] \cdot \mathbf{s}) \hat{\sigma}_s(\zeta) d\zeta \quad (47)$$

where $\Sigma_{t,e} = \Sigma_t \cap V_e^h$, $\{\cdot\}$ denotes the averaged quantity obtained from the two crack faces Σ^\pm , e.g. $\{\boldsymbol{\sigma}\} = \frac{1}{2}(\boldsymbol{\sigma}^+ + \boldsymbol{\sigma}^-)$, and $[[\mathbf{v}]] = (\mathbf{v}^+ - \mathbf{v}^-)$ denotes the jump of \mathbf{v} across the crack.

3.2.2. Shape functions

As before, enrichment for the displacement is chosen in order to guarantee that all nodes of the elements in the set \mathcal{K} are located within the distance ρ from the closest crack tip. Hence the displacement shape functions (44) do not involve Heaviside enrichment in the domain $\cup_{e \in \mathcal{K}} V_e^h$. The stress in each element V_e^h , $e \in \mathcal{K}$, is represented by the four singular functions $\{\psi_j^\sigma\}$ given in (42) and by standard Lagrange basis functions. The finite-dimensional space H^{-1h} is defined as follows:

$$H^{-1h} = \left\{ \begin{aligned} &\cup_{e \in \mathcal{K}} v^e(\mathbf{x}) : v^e(\mathbf{x}) = \sum_{i \in I_e} a_i^e N_i(\mathbf{x}) + \sum_{i \in I_e} N_i(\mathbf{x}) \sum_{j=1}^4 c_i^{j,e} (\psi_j^\sigma(\mathbf{x}) \\ &- \psi_j^\sigma(\mathbf{x}_i)) \text{ if } \mathbf{x} \in V_e^h; v^e(\mathbf{x}) = 0 \text{ if } \mathbf{x} \notin V_e^h \end{aligned} \right\}$$

where $\mathbf{x} \in \cup_{e \in \mathcal{K}} V_e^h \setminus \Sigma$; $a_i^e, c_i^{j,e} \in \mathbb{R}$; and I_e denotes the set of all nodes in element e .

3.3. Infinite elements

In modeling hydraulic fracture propagation in large-scale problems, the boundary conditions at a finite outer boundary are often unknown. This can be resolved by modeling a fracture propagation in an infinite domain, assuming a vanishing displacement at infinity. To represent an infinite domain, we employ mapped infinite elements that make it possible to capture a decaying far-field displacement [38,39]. The details of the infinite elements used in this paper are summarized in Appendix B.

4. Coupling schemes

We considered a number of different strategies of varying complexity to couple the XFEM framework with the fluid flow equations in order to model propagating hydraulic fractures. However, only the $P \rightarrow W$ scheme and the P&W scheme were found to be suitable. Given that the XFEM, with the appropriate enrichment, can resolve the Neumann to Dirichlet map with $O(h^2)$ accuracy, the $P \rightarrow W$ scheme (in which the XFEM uses nodal pressures Π_i as Neumann boundary conditions to determine the nodal crack widths Ω_i) would seem a natural choice. However, the $P \rightarrow W$ scheme will only work for situations in which there is a finite fluid lag and cannot be used if the fluid and fracture fronts

coalesce. When there is a finite fluid lag the separation of the fluid front γ_f from the fracture front γ significantly simplifies the coupling strategy that is required. In this case, the fluid pressure tends to zero at γ_f while there is zero or finite pressure in the fluid lag region, so that the fracture growth is governed by the standard $\Omega \sim \hat{\zeta}^{1/2}$ asymptote of LEFM. When the two fronts coalesce the pressure field is typically singular at the tip, which complicates the numerical approximation process considerably. Unfortunately, the asymptotic solution for this singular pressure field cannot be used by the $P \rightarrow W$ scheme, since the domain of validity of this asymptotic expansion is extremely small $\lesssim 1\%$ of the fracture length. Because the domain of validity of the corresponding asymptotic expansion for the tip widths is much larger and extends to $\sim 10\%$ of the fracture length, it is natural to consider a $W \rightarrow P$ scheme (in which the XFEM uses the nodal widths Ω_i as Dirichlet boundary conditions to determine the nodal pressures Π_i). However, the XFEM, even with the appropriate enrichment, can only resolve the Dirichlet to Neumann map with $O(h)$ accuracy. In addition, spurious parasitic modes due to the blending corrupt the pressure field near the transition from the tip to Heaviside enrichment regions. Thus in order to arrive at a scheme that combines the $O(h^2)$ accuracy of the ND map with the larger domain of validity of the width asymptotic expansion in the tips, we developed the P&W scheme. In the P&W scheme, the XFEM uses nodal widths $\Omega_{t,i}$ from the asymptotic solution at the crack tip and nodal pressures Π_i as Neumann boundary conditions in the interior part of the crack away from the tips, which we refer to as the *channel region*, and solves for the nodal widths within this channel region (see Section 3). In this way the P&W scheme can employ the asymptotic width as the boundary condition at the crack tip.

An important component of any HF coupling scheme is a strategy to locate the free boundaries in the problem. Typically there exist a multiplicity of pairs (Ω, Π) that equilibrate and satisfy the fluid conservation equations, which may be regarded as being parameterized by the location of the free boundaries (γ_f, γ) . In order to identify the desired solution it is crucial that the coupling algorithm be able to determine γ_f and γ accurately. In the case of a finite lag, (i.e., $\gamma_f < \gamma$), γ_f can be determined by solving the evolution equation (32) using the Forward Euler method, while γ can be determined by imposing the $\hat{\zeta}^{1/2}$ asymptote of LEFM. In the case of zero lag, (i.e., $\gamma_f = \gamma$), one possibility is to solve the evolution equation (32), which provides an expression for the combined front velocity. However, because of the singular pressure field, solving (32) involves evaluating a distinguished limit numerically – a process that is notoriously susceptible to round-off errors. In this case, some form of implicit scheme is required to locate the fracture free boundary that does not depend directly on (32). In this paper, we use a fairly simple device in which a fracture growth increment $\Delta\gamma$ in a given direction is prescribed and the corresponding time increment $\Delta\tau$ is determined so that the coupled equations and the applicable propagation condition are both satisfied, which thereby locates the free boundary in space–time. This approach has the advantage that the fracture front only has to be moved once per growth increment, which means that the tip enrichment only needs to be updated once per growth increment resulting in significant computational savings. However, for more complex situations, such as non-symmetric fracture growth, this scheme will not work as fixed spatial growth increments on different fronts will then not necessarily occur at the same time. Though the above scheme suffices for the purposes of this paper, more complex situations will require more generally applicable algorithms such as the implicit level set scheme [24], which exploits the local tip asymptotic behavior to locate the free boundary in space.

In this paper we assume that the fracture grows symmetrically at both crack tips. The general algorithm, which follows those presented in [40,41], starts with a crack of an initial half-length γ_0 , at

which point the pair (Ω, Π) is initialized to an available reference solution such as an early time solution for an initially straight crack. At step M of the algorithm, $M \geq 1$, the crack growth is simulated by adding a crack increment of a fixed length $\Delta\gamma_M$ to each crack tip, inclined at a given deflection angle θ_M to the current propagation direction. Thus, the crack half-length at step M is given by $\gamma_M = \gamma_0 + \sum_{i=1}^M \Delta\gamma_i$. For this new crack configuration, the algorithm determines: the corresponding time $\tau_M = \tau_{M-1} + \Delta\tau_M$, the crack width $\Omega(\zeta, \tau_M)$, the pressure $\Pi(\zeta, \tau_M)$, and the location of the fluid front γ_{fM} for a problem with fluid lag, so that the coupled governing equations (24)–(35) are satisfied. Based on the solution at time-step M , the new deflection angle θ_{M+1} is determined that defines the propagation direction for time-step $M + 1$.

At each step of the simulation, the structure of the Heaviside and the crack tip enrichments is introduced as described in Section 3. The radius of the tip enrichment is a fixed pre-defined parameter ρ . To discretize the governing equations for nodal values of the crack width $\Omega_i = \Omega(\zeta_i, \tau_M)$, the nodes $\zeta = \zeta_i$ are chosen at the intersections of the crack with the edges of the finite element mesh (see Fig. 2). The nodes along the crack are numbered consecutively, by $\zeta_0, \dots, \zeta_{N+1}$, where $-\gamma = \zeta_0$ and $\gamma = \zeta_{N+1}$ are the locations of the crack tips. The nodal widths are abbreviated into the vector $\Omega = (\Omega_1, \dots, \Omega_N)^T$. We denote the nodal net pressures by $\Pi_i = \Pi(\zeta_i, \tau_M)$ and the nodal fluid pressures by $\Pi_i^f = \Pi_i + \hat{\sigma}_n(\zeta_i)$.

Each scheme we consider below employs an approximation of the pressure and the width by basis functions, which are defined in terms of the standard piecewise linear Lagrange hat functions associated with the nodes ζ_i

$$h_i(\zeta) = \begin{cases} \frac{\zeta - \zeta_{i-1}}{\zeta_i - \zeta_{i-1}}, & \text{if } \zeta_{i-1} \leq \zeta < \zeta_i \\ \frac{\zeta_{i+1} - \zeta}{\zeta_{i+1} - \zeta_i}, & \text{if } \zeta_i \leq \zeta < \zeta_{i+1} \\ 0, & \text{else} \end{cases} \quad (48)$$

4.1. $P \rightarrow W$ scheme for a crack with fluid lag

In this section we consider a crack partially filled with fluid so that the width in the crack tip is governed by the toughness asymptote (34). At time τ_M , the fluid front is located at $\gamma_{fM} < \gamma_M$. The crack is divided into two fluid lag regions $(-\gamma, -\gamma_f)$ and (γ_f, γ) , i.e., one for each wing of the crack), and the fluid-filled region $(-\gamma_f, \gamma_f)$ (designated by the shaded region), which contains the channel region $(-\gamma_c, \gamma_c)$ (see Fig. 2). Each of the two lag regions includes m finite elements, $m \geq 1$, starting with the element containing the crack tip and including an element that is partially filled with fluid. The elements that are cut by the crack and are completely fluid-filled form the so-called channel. The nodes ζ_m and ζ_{N-m+1} are located at the channel boundaries. The problem is reduced to finding unknown nodal fluid pressures in the channel, abbreviated below into a vector $\Pi_c^f = (\Pi_m^f, \dots, \Pi_{N-m+1}^f)^T$.

4.1.1. Pressure and width basis functions

The present scheme employs the XFEM to provide the nodal crack widths Ω , given the nodal channel fluid pressures Π_c^f . This

link between the vectors Π_c^f and Ω can be constructed by means of a linear operator D :

$$\Omega = D\Pi_c^f + \hat{\Omega} \quad (49)$$

where $\hat{\Omega}$ is the vector of nodal widths that results from the solution of the elasticity problem (24)–(27) augmented by the boundary condition, in which the tractions along the crack are given by the normal and shear stresses induced by the external state of stress:

$$\sigma_n^+ = \sigma_n^- = \hat{\sigma}_n(\zeta), \quad \sigma_s^+ = \sigma_s^- = \hat{\sigma}_s(\zeta), \quad \text{for } \zeta \in \Sigma \quad (50)$$

The crack width resulting from the solution of this elasticity problem at any point ζ along the crack is denoted $\hat{\Omega}(\zeta)$. Eq. (49) represents the superposition of the crack width induced by the fluid pressure within the crack and the crack width induced by the external state of stress.

We approximate the net pressure $\Pi(\zeta, \tau_M)$ in the fluid-filled portion of the crack by a linear combination of pressure basis functions $P_i(\zeta)$ ($i = m : N - m + 1$) as follows,

$$\Pi(\zeta, \tau_M) \approx \sum_{i=m}^{N-m+1} \Pi_i^f P_i(\zeta) - \hat{\sigma}_n(\zeta) \quad (51)$$

where the basis functions $P_i(\zeta)$ for $i = m + 1 : N - m$ are the hat functions defined in (48), i.e.,

$$P_i(\zeta) = h_i(\zeta), \quad i = m + 1 : N - m \quad (52)$$

Within the partially-filled elements the basis functions $P_i(\zeta)$ for $i = m, N - m + 1$ are hat functions that vanish at the fluid fronts $\pm\gamma_f$:

$$P_m(\zeta) = \begin{cases} \frac{\zeta + \gamma_f}{\zeta_m + \gamma_f}, & \text{if } -\gamma_f \leq \zeta < \zeta_m \\ h_m(\zeta), & \text{if } \zeta_m \leq \zeta < \zeta_{m+1} \\ 0, & \text{else} \end{cases} \quad (53)$$

$$P_{N-m+1}(\zeta) = \begin{cases} \frac{\zeta - \gamma_f}{\zeta_{N-m+1} - \gamma_f}, & \text{if } \zeta_{N-m+1} \leq \zeta < \gamma_f \\ h_{N-m+1}(\zeta), & \text{if } \zeta_{N-m} \leq \zeta < \zeta_{N-m+1} \\ 0, & \text{else} \end{cases} \quad (54)$$

Functions (52)–(54) satisfy the Kronecker δ property, $P_i(\zeta_j) = \delta_{ij}$, for $i, j = m : N - m + 1$, so that the value of the approximated pressure $\Pi(\zeta, \tau_M)$ at ζ_i is equal to the nodal net pressure Π_i for $i = m : N - m + 1$.

The XFEM can be used to solve the elasticity problem (24)–(27) complemented by the boundary condition, in which the pressure along the crack is given by a pressure basis function $P_i(\zeta)$ ($i = m : N - m + 1$):

$$\sigma_n^+ = \sigma_n^- = -P_i(\zeta), \quad \sigma_s^+ = \sigma_s^- = 0, \quad \text{for } \zeta \in \Sigma \quad (55)$$

For consistency with the toughness asymptote, the square-root enrichment $\lambda = 1/2$ must be used by the XFEM formulation in this case. The solution of this elasticity problem yields the corresponding width basis functions, which we denote by $\omega_i(\zeta)$.

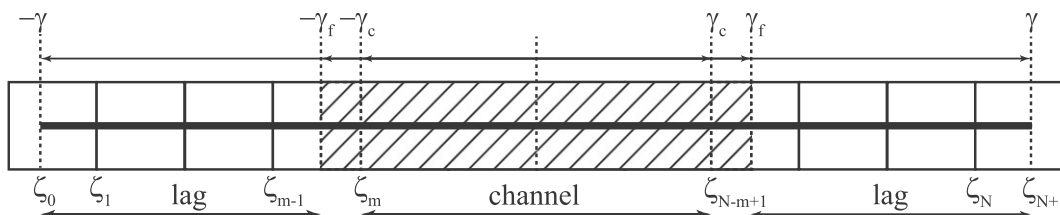


Fig. 2. Discretization of a crack with a fluid lag within the regular FEM mesh. The lag regions $(-\gamma, -\gamma_f)$ and (γ_f, γ) and the channel region $(-\gamma_c, \gamma_c)$ are indicated while the fluid-filled region $(-\gamma_f, \gamma_f)$ is designated by the shading.

Due to the linearity of the elasticity problem, the width $\Omega(\zeta, \tau_M)$ along the crack corresponding to the pressure (51) is given by the linear combination of the width basis functions,

$$\Omega(\zeta, \tau_M) \approx \sum_{i=m}^{N-m+1} \Pi_i^f \omega_i(\zeta) + \hat{\Omega}(\zeta) \quad (56)$$

The nodal width Ω_i can thus be found as

$$\Omega_i = \sum_{j=m}^{N-m+1} \Pi_j^f \omega_j(\zeta_i) + \hat{\Omega}_i \quad (57)$$

in which the expansion coefficients are not nodal widths, but are the nodal fluid pressures Π_j^f . Eq. (57) can be interpreted as a component form of (49) in which the linear operator D is given by its components

$$D_{ij} = \omega_j(\zeta_i), \quad i = 1 : N; \quad j = m : N - m + 1 \quad (58)$$

4.1.2. Discretization of the fluid flow equations

The fluid flow equations are reformulated in a weak form as follows. Let $\phi(\zeta)$ be a test function defined in the channel, $\zeta \in (-\gamma_c, \gamma_c)$. Using integration by parts applied to the integral $\int_{-\gamma_c}^{\gamma_c} \phi(\zeta) \dot{\Omega} d\zeta$, the conservation law (31) can be reformulated as

$$\begin{aligned} \int_{-\gamma_c}^{\gamma_c} \phi(\zeta) \dot{\Omega} d\zeta &= -\phi(\gamma_c) \Psi(\gamma_c) + \phi(-\gamma_c) \Psi(-\gamma_c) \\ &+ \int_{-\gamma_c}^{\gamma_c} \phi'(\zeta) \Psi d\zeta + \phi(0) \end{aligned} \quad (59)$$

At step M of the algorithm, the time derivative $\dot{\Omega}$ is approximated by the backward difference approximation

$$\dot{\Omega} = \frac{\Omega(\zeta, \tau_{M-1} + \Delta\tau) - \Omega(\zeta, \tau_{M-1})}{\Delta\tau} \quad (60)$$

where $\Delta\tau = \tau_M - \tau_{M-1}$ is the unknown time-step. For brevity, we denote all quantities obtained at the previous time-step by the subscript or the superscript o ; e.g. $\tau_o = \tau_{M-1}$ and $\Omega^o = \Omega(\zeta, \tau_{M-1})$, while quantities without sub or superscripts are assumed to be evaluated at time τ_M , i.e., $\Omega = \Omega(\zeta, \tau_M)$.

By substituting the time derivative into (59) and using Poiseuille's law (30), we obtain

$$\begin{aligned} \int_{-\gamma_c}^{\gamma_c} \phi(\zeta) \dot{\Omega} d\zeta &= \int_{-\gamma_c}^{\gamma_c} \phi(\zeta) \Omega^o d\zeta + \Delta\tau (-\phi(\gamma_c) \Psi(\gamma_c) \\ &+ \phi(-\gamma_c) \Psi(-\gamma_c) + \phi(0)) - \Delta\tau \int_{-\gamma_c}^{\gamma_c} \phi'(\zeta) \Omega^3 \frac{\partial \Pi^f}{\partial \zeta} d\zeta \end{aligned} \quad (61)$$

Assuming that the pressure and the width are given by combinations of the basis functions (51) and (56) and using the pressure basis functions $P_i(\zeta)$ for $i = m : N - m + 1$ as the test function $\phi(\zeta)$, (61) can be rewritten for $i = m : N - m + 1$ as follows

$$\begin{aligned} \sum_{j=m}^{N-m+1} \Pi_j^f \int_{-\gamma_c}^{\gamma_c} P_i(\zeta) \omega_j(\zeta) d\zeta &= \int_{-\gamma_c}^{\gamma_c} P_i(\zeta) (\Omega^o - \hat{\Omega}) d\zeta \\ &+ \Delta\tau (-P_i(\gamma_c) \Psi(\gamma_c) \\ &+ P_i(-\gamma_c) \Psi(-\gamma_c) + P_i(0)) \\ &- \Delta\tau \sum_{j=m}^{N-m+1} \Pi_j^f \int_{-\gamma_c}^{\gamma_c} P_i(\zeta) \Omega^3 P_j'(\zeta) d\zeta \end{aligned} \quad (62)$$

Further, we define the mass matrix \mathbf{M} and a tri-diagonal matrix \mathbf{A} , both having dimensions $(N - 2m + 2) \times (N - 2m + 2)$, by

$$M_{ij} = \int_{-\gamma_c}^{\gamma_c} P_i(\zeta) \omega_j(\zeta) d\zeta, \quad i, j = m : N - m + 1 \quad (63)$$

$$A_{ij} = - \int_{-\gamma_c}^{\gamma_c} P_i'(\zeta) \Omega^3 P_j'(\zeta) d\zeta, \quad i, j = m : N - m + 1 \quad (64)$$

The integrals in the entries of both matrices are computed numerically. To compute the matrix \mathbf{A} , the crack width Ω is reconstructed from the expansion (56).

Thus, the weak form (62) of the fluid flow equations can be rewritten in a discretized form as a system of nonlinear algebraic equations for the vector Π_c^f of unknown nodal fluid pressures as

$$(\mathbf{M} - \Delta\tau \mathbf{A}) \Pi_c^f = \mathbf{F} \quad (65)$$

where the components of the vector \mathbf{F} are

$$\begin{aligned} F_i &= \int_{-\gamma_c}^{\gamma_c} P_i(\zeta) (\Omega^o - \hat{\Omega}) d\zeta + \Delta\tau (-P_i(\gamma_c) \Psi(\gamma_c) \\ &+ P_i(-\gamma_c) \Psi(-\gamma_c) + P_i(0)) \end{aligned} \quad (66)$$

In the numerical examples presented in this paper the applied shear stress is zero, i.e., $\sigma_s = 0$. The boundary fluxes $\Psi(\pm\gamma_c)$ involved in (66) characterize the exchange of fluid volume outside the channel boundaries, over the time-step $\Delta\tau$. The flux $\Psi(\gamma_c)$ is computed from

$$\Psi(\gamma_c) = \frac{1}{\Delta\tau} \int_{\gamma_c}^{\gamma_f} (\Omega - \Omega^o) d\zeta \quad (67)$$

and the flux $\Psi(-\gamma_c)$ is found similarly. The non linearity in the system (65) arises from the dependence of the matrix \mathbf{A} and the right hand side vector \mathbf{F} (via (67)) on the crack width Ω , and thus on the fluid pressures Π_c^f via (49). The primary unknown in this scheme is the vector of nodal fluid pressures Π_c^f .

4.1.3. Time-step and deflection-angle determination

Following the scheme introduced by Gordeliy and Detournay [42,40] and Bungler et al. [41] for flat and curved cracks with fluid lag, the condition for finding the unknown time-step $\Delta\tau$ can be imposed by enforcing the propagation criterion at the crack tip, from which the time-step is found as a root of an implicit function $f(\Delta\tau)$:

$$f(\Delta\tau) = 0 \quad (68)$$

When the crack grows along its initial direction due to symmetry in stress distribution around the crack tip, the deflection angle can be set to zero, $\theta_{M+1} = 0$. To construct $f(\Delta\tau)$ in simulations performed for a flat crack with fluid lag (Section 5.1), one can apply the tip asymptote (34) in a weak form over the tip element as follows:

$$f(\Delta\tau) = \int_{\zeta_N}^{\gamma} \Omega d\zeta - \frac{2}{3} \mathcal{K}(\gamma - \zeta_N)^{3/2} \quad (69)$$

This function f depends on $\Delta\tau$ via the solution Ω obtained for the current time-step $\Delta\tau$.

To model a curving crack, the propagation criterion may be chosen according to the maximum tensile stress criterion [43]:

$$f(\Delta\tau) = \mathcal{K} - \cos\left(\frac{\theta_{M+1}}{2}\right) \left(\mathcal{K}_I \cos^2\left(\frac{\theta_{M+1}}{2}\right) - \frac{3}{2} \mathcal{K}_{II} \sin \theta_{M+1} \right) \quad (70)$$

in which \mathcal{K}_I and \mathcal{K}_{II} are the dimensionless mode I and II stress intensity factors corresponding to the behavior of the dimensionless normal and shear displacement jumps near the crack tip. The deflection angle is defined by Erdogan and Sih [43]

$$\theta_{M+1} = 2 \arctan \left(\frac{\mathcal{K}_I \pm \sqrt{\mathcal{K}_I^2 + 8\mathcal{K}_{II}^2}}{4\mathcal{K}_{II}} \right) \quad (71)$$

in which the sign is chosen so that the tensile stress normal to the deflection direction ahead of the crack tip, which is proportional to the second term on the right of (70), achieves its maximum value. The function f in (70) depends on $\Delta\tau$ via the stress intensity factors \mathcal{K}_I and \mathcal{K}_{II} obtained for the current time-step $\Delta\tau$. For the numerical examples presented in this paper, the stress intensity factors were computed using a domain form of the interaction integral, which is outlined in Appendix A.

4.1.4. Fluid front location

The fluid front is located by applying the Forward Euler scheme to the evolution equation (32)

$$\gamma_f = \gamma_f^o + \Delta\tau V_f$$

where γ_f^o is the location of the front at the previous time τ_o and V_f is the fluid front velocity determined from (32) and evaluated at $\zeta = \gamma_c$,

$$V_f = -\Omega(\gamma_c)^2 \frac{\partial \Pi^f}{\partial \zeta} \Big|_{\gamma_c} \quad (72)$$

The pressure gradient required in (72) can be computed by fitting a polynomial to the nodal pressures Π_i^f , including the pressure $\Pi^f(\gamma_f) = 0$, and finding the gradient of the polynomial at $\zeta = \gamma_c$. For the numerical examples in this paper, the pressure gradient was computed by fitting either a quadratic or a cubic polynomial to the pressures Π_i^f ($i = N - m - 1, \dots, N - m + 1$) and $\Pi^f(\gamma_f)$, which are equivalent to second or third order backward difference approximations.

To accelerate the convergence of the iterative scheme in the numerical examples in Sections 5.1 and 5.2, we use a Picard relaxation scheme for the velocity at successive iterates. Thus for the j th iteration of the fluid front, we use the following expression for the fluid velocity

$$V_f^{(j)} = \chi V_f^{(j-1)} - (1 - \chi) \Omega(\gamma_c)^2 \frac{\partial \Pi^f}{\partial \zeta} \Big|_{\gamma_c} \quad (73)$$

where $0 < \chi < 1$ is the relaxation parameter. The iterations are run until convergence is reached within a pre-defined relative tolerance δ_f ,

$$|\gamma_f^{(j)} - \gamma_f^{(j-1)}| < \delta_f \gamma_f^{(j-1)} \quad (74)$$

where $\gamma_f^{(j)}$ is the fluid front at iteration j .

4.1.5. Iterative solution of the coupled equations

We describe the iterative algorithm that uses the $P \rightarrow W$ scheme to solve for: the time τ_M (or equivalently the time-step $\Delta\tau_M$), the location of the fluid front γ_{fM} , the crack width $\Omega(\zeta, \tau_M)$, and the pressure $\Pi(\zeta, \tau_M)$, given the crack length γ_M at the simulation step M . For a curving crack, the algorithm also determines the deflection angle θ_{M+1} for the new crack growth increment. This algorithm uses the same logic to locate the fluid front and to determine the time-step as that used in [42,40,41].

For a fixed crack configuration corresponding to the crack tip at $\zeta = \gamma_M$, and for a trial location of the fluid front, the width basis functions $\omega_i(\zeta)$ are obtained for $i = m : N - m + 1$ from the XFEM solutions for the elasticity problems, in which the pressures along the crack are given by the pressure basis functions $P_i(\zeta)$ defined in (52)–(54). The mass matrix \mathbf{M} is constructed using these width basis functions, according to (63).

For each trial location of the fluid front, the secant method is used to solve the nonlinear equation (68) for the time-step $\Delta\tau$. For each value of the time-step involved, the system (65) is solved by fixed point iteration to yield the nodal fluid pressures Π_c^f in the

channel region. At iteration k , $\Pi_c^{f,(k)}$ is determined by solving the linear system:

$$(\mathbf{M} - \Delta\tau \mathbf{A}^{(k-1)}) \Pi_c^{f,(k)} = \mathbf{F}^{(k-1)}$$

in which the superscripts (k) and $(k-1)$ denote the quantities at current and previous iterations. The crack width $\Omega(\zeta)$, required for the construction of the function f in (68), is found from the channel fluid pressures Π_c^f via (56).

When the iterations for the nodal pressures and the time-step reach a desired tolerance, the fluid front location is updated via (73). The iterative procedure for locating the fluid front, the time-step, and the nodal pressures runs until a desired tolerance has been obtained. Then the stress intensity factors are computed and the deflection angle θ_{M+1} for the new crack increment of length $\Delta\gamma_{M+1}$ is found from (71).

4.2. P&W scheme for cracks with singular tip pressures

The P&W XFEM scheme described above makes it possible to incorporate the asymptotic behavior of the width in the neighborhood of the crack tip as a boundary condition. The advantage of this scheme is that it can treat problems in which the fluid pressure is singular at the crack tips, such as the viscous mode of crack propagation [27,16]. In order to facilitate comparison with published reference solutions we only consider the propagation of cracks along straight lines, so that the deflection angle at each step of propagation is zero, i.e., $\theta_M = 0$. This assumption does not limit the class of problems that can be solved using the coupled P&W scheme. Indeed, this restriction can be relaxed by incorporating an appropriate search strategy (e.g., for the maximum tensile stress direction in the vicinity of the crack tip) to identify the propagation direction of the crack at each growth increment. For the problems we consider, we also assume that the shear stress applied along the crack faces vanishes: i.e., $\hat{\sigma}_s = 0$. Non-zero applied shear stress fields $\hat{\sigma}_s$ can easily be incorporated using superposition as was done for the $P \rightarrow W$ scheme in Section 4.1.

Though the coupled P&W scheme can easily be applied to problems with fluid lag (i.e., $\gamma_f < \gamma$), the additional complexity of this scheme compared to the $P \rightarrow W$ scheme is unwarranted in this case. Therefore for the presentation of the coupled P&W scheme we consider cracks that are completely filled with fluid, i.e., $\gamma_f = \gamma$, for which the $P \rightarrow W$ scheme does not work. The crack is divided into two crack tip regions and a channel region (see Fig. 3). Each of the two tip regions includes n finite elements, $n \geq 1$, counting from the element containing the crack tip. The width in the crack tip zone is assumed to be governed by the tip asymptote (34) or (35). Thus the XFEM uses the crack width boundary condition (28) in the tip regions $(\zeta_0, \zeta_n) \cup (\zeta_{N-n+1}, \zeta_{N+1})$, and the pressure boundary condition (29) in the channel region (ζ_n, ζ_{N-n+1}) . It is assumed that blending of the two enrichments takes place in the channel. Hence we choose the tip enrichment radius ρ so that elements for which tip enrichment is applied completely cover the tip regions (ζ_0, ζ_n) and $(\zeta_{N-n+1}, \zeta_{N+1})$.

4.2.1. The XFEM solution

The XFEM solution can be represented as a superposition of solutions that approximate the width boundary condition (28) and the pressure boundary condition (29). The aim is to use the nodal net pressures Π_i in the channel and the asymptotic widths in the tips to reconstruct the appropriate boundary conditions (28) and (29) for the XFEM.

Since the crack is assumed to propagate along a straight line, the applied normal stress $\hat{\sigma}_n(\zeta) \equiv \hat{\sigma}_n$ is uniform along the crack and the fluid flow equations (30), (32) and (36) can be reformulated in terms of the gradient of the net pressure $\frac{\partial \Pi}{\partial \zeta} = \frac{\partial \Pi^f}{\partial \zeta}$.

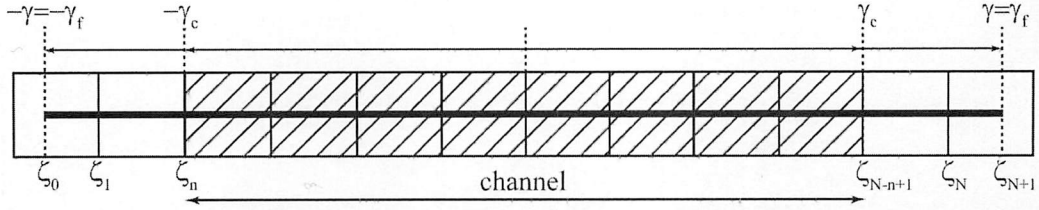


Fig. 3. Discretization of the crack without fluid lag within the regular FEM mesh. The elements in the channel region are shaded while there are $n = 2$ elements in the tip regions.

To obtain a smooth representation of the net pressure Π in the channel, we use the Hermite cubic basis functions H_i^0 , associated with the nodal values Π_i , and H_i^1 , associated with the nodal derivatives Π'_i [32]:

$$\Pi(\zeta, \tau_M) \approx \sum_{i=n}^{N-n+1} (\Pi_i H_i^0(\zeta) + \Pi'_i H_i^1(\zeta)), \quad \zeta \in (\zeta_n, \zeta_{N-n+1}) \quad (75)$$

Expressions for the basis functions H_i^0 and H_i^1 are given in Appendix C. Expression (75) provides a C^1 -continuous approximation of Π in the channel.

In the tip regions, the crack width is approximated by the tip asymptote according to (34) or (35). This asymptote as the distance ζ from the tip tends to zero can be expressed in the following general form, that involves the fracture front velocity $\dot{\gamma}(\tau)$:

$$\Omega \sim \mathcal{W}(\zeta; \dot{\gamma}), \quad \zeta \rightarrow 0 \quad (76)$$

The front velocity can be approximated by $\dot{\gamma} \approx \Delta\gamma_M/\Delta\tau$, where $\Delta\tau$ is the unknown time-step that has to be determined in the coupled solution.

The crack width in the tip regions is then approximated by

$$\begin{aligned} \Omega(\zeta, \tau_M) \approx & \mathcal{W}(\zeta_{N+1} - \zeta_{N-n+1}; \dot{\gamma}) \left(\frac{\zeta_{N+1} - \zeta}{\zeta_{N+1} - \zeta_{N-n+1}} \right)^\lambda H(\zeta - \zeta_{N-n+1}) \\ & + \mathcal{W}(\zeta_n - \zeta_0; \dot{\gamma}) \left(\frac{\zeta - \zeta_0}{\zeta_n - \zeta_0} \right)^\lambda H(\zeta_n - \zeta), \quad \zeta \in (\zeta_0, \zeta_n) \cup (\zeta_{N-n+1}, \zeta_{N+1}) \end{aligned}$$

where again H is the Heaviside function. Above, λ is the power-law exponent that corresponds to the asymptote (34) or (35). The same power-law exponent is employed for the singular tip enrichment within the XFEM.

The elasticity problem (24)–(27) is solved using the XFEM for the following set of boundary conditions along the crack:

(a) The XFEM is used to generate $2(N - 2n + 2)$ width basis functions denoted by $\omega_i^p(\zeta)$ that are the solutions to the elasticity problem in which the prescribed pressures are given by the Hermite basis function $H_i^p(\zeta)$ for $i = n : N - n + 1$ and for $p = 0, 1$:

$$\sigma_n^+ = \sigma_n^- = -H_i^p(\zeta), \quad \zeta \in \Sigma_c; \quad \sigma_s^+ = \sigma_s^- = 0, \quad \zeta \in \Sigma; \quad [[\mathbf{u}]]_\Sigma \cdot \mathbf{n} = 0, \quad \zeta \in \Sigma_t \quad (77)$$

(b) The XFEM is used to generate the width basis function denoted by $\omega_0(\zeta)$ in which the crack width is given by the power-law basis function consistent with the asymptote in the tip region $\zeta \in (\zeta_0, \zeta_n)$ and zero pressure elsewhere:

$$[[\mathbf{u}]]_\Sigma \cdot \mathbf{n} = \left(\frac{\zeta - \zeta_0}{\zeta_n - \zeta_0} \right)^\lambda H(\zeta_n - \zeta), \quad \text{for } \zeta \in \Sigma_t \quad (78)$$

$$\sigma_n^+ = \sigma_n^- = 0, \quad \text{for } \zeta \in \Sigma_c \quad (79)$$

$$\sigma_s^+ = \sigma_s^- = 0, \quad \text{for } \zeta \in \Sigma \quad (80)$$

(c) The XFEM is used to generate the width basis function denoted by $\omega_{N+1}(\zeta)$ in which the crack width is given by the power-law basis function consistent with the asymptote in the tip region $\zeta \in (\zeta_{N-n+1}, \zeta_{N+1})$ and zero pressure elsewhere:

$$[[\mathbf{u}]]_\Sigma \cdot \mathbf{n} = \left(\frac{\zeta_{N+1} - \zeta}{\zeta_{N+1} - \zeta_{N-n+1}} \right)^\lambda H(\zeta - \zeta_{N-n+1}), \quad \text{for } \zeta \in \Sigma_t \quad (81)$$

$$\sigma_n^+ = \sigma_n^- = 0, \quad \text{for } \zeta \in \Sigma_c \quad (82)$$

$$\sigma_s^+ = \sigma_s^- = 0, \quad \text{for } \zeta \in \Sigma \quad (83)$$

The solution of the elasticity problem (24)–(27), complemented by the boundary condition (28) in the tip regions $(\zeta_0, \zeta_n) \cup (\zeta_{N-n+1}, \zeta_{N+1})$ and by the boundary condition (29) in the channel (ζ_n, ζ_{N-n+1}) , can be approximated by the superposition of the XFEM solutions described in (a)–(c) above. Note that zero shear stress along the complete crack is enforced in (a)–(c). The crack width Ω corresponding to this superposition is obtained as

$$\begin{aligned} \Omega(\zeta, \tau_M) \approx & \sum_{i=n}^{N-n+1} (\Pi_i \omega_i^0(\zeta) + \Pi'_i \omega_i^1(\zeta)) + \mathcal{W}(\zeta_n - \zeta_0; \dot{\gamma}) \omega_0(\zeta) \\ & + \mathcal{W}(\zeta_{N+1} - \zeta_{N-n+1}; \dot{\gamma}) \omega_{N+1}(\zeta), \quad \zeta \in \Sigma \end{aligned} \quad (84)$$

Hence when the nodal pressures Π_i and the nodal derivatives Π'_i are given, (84) provides the XFEM approximation for the nodal widths in the channel,

$$\begin{aligned} \Omega_i = & \sum_{j=n}^{N-n+1} (\Pi_j \omega_j^0(\zeta_i) + \Pi'_j \omega_j^1(\zeta_i)) + \mathcal{W}(\zeta_n - \zeta_0; \dot{\gamma}) \omega_0(\zeta_i) \\ & + \mathcal{W}(\zeta_{N+1} - \zeta_{N-n+1}; \dot{\gamma}) \omega_{N+1}(\zeta_i), \quad i \\ = & n : N - n + 1 \end{aligned} \quad (85)$$

4.2.2. Discretization of the fluid flow equations

The fluid flow equations in this case can be discretized using a collocation scheme. The conservation law (31) and Poiseuille's law (30) can be rewritten as follows:

$$\frac{\partial \Psi}{\partial \zeta} = F_\Psi(\zeta; \Omega, \Delta\tau) \quad (86)$$

$$\frac{\partial \Pi}{\partial \zeta} = F_\Pi(\zeta; \Psi, \Omega) \quad (87)$$

in which

$$F_\Psi(\zeta; \Omega, \Delta\tau) = \delta(\zeta) - \dot{\Omega}, \quad F_\Pi(\zeta; \Psi, \Omega) = -\Psi \Omega^{-3} \quad (88)$$

The time derivative involved in F_Ψ is approximated via (60); thus F_Ψ is a function of the crack width Ω and the time-step $\Delta\tau$.

The ODE (86) can be integrated over the interval (ζ_i, ζ_{i+1}) for $i = n : N - n$ using the trapezoidal rule applied to the integral of $\dot{\Omega}$,

$$\Psi_{i+1} - \Psi_i = \int_{\zeta_i}^{\zeta_{i+1}} F_\Psi(\zeta) d\zeta = \Delta\tau_0 - \frac{\Delta\zeta_i}{2} (\dot{\Omega}_i + \dot{\Omega}_{i+1}) + O(\Delta\zeta^3) \quad (89)$$

where $\Delta\zeta_i = \zeta_{i+1} - \zeta_i$ and $\Delta\zeta = \max_{i=n:N-n} \Delta\zeta_i$, and

$$\Delta_{i0} = \begin{cases} 1 & \text{if } 0 \in (\zeta_i, \zeta_{i+1}) \\ \frac{1}{2} & \text{if } 0 = \zeta_{i+1} \\ -\frac{1}{2} & \text{if } 0 = \zeta_i \\ 0 & \text{if } 0 \notin [\zeta_i, \zeta_{i+1}] \end{cases}$$

The arguments Ω and $\Delta\tau$ in the function F_Ψ are omitted for brevity. Similarly, (87) is integrated over (ζ_i, ζ_{i+1}) for $i = n : N - n$ as

$$\Pi_{i+1} - \Pi_i = \frac{\Delta\zeta_i}{2} (F_\Pi(\zeta_i) + F_\Pi(\zeta_{i+1})) + O(\Delta\zeta^3) \quad (90)$$

4.2.3. Iterative solution of the coupled equations

Given the crack length γ_M at the simulation step M , the iterative solution is obtained for the time-step $\Delta\tau$, as well as for the following nodal quantities in the channel, comprising: the crack widths Ω_i , the pressures Π_i , and the fluxes Ψ_i (for $i = n : N - n + 1$). This leads to $3(N - 2n + 2) + 1$ unknowns. Eqs. (85), (89) and (90) provide $3(N - 2n + 2) - 2$ equations.

The remaining three equations are provided by the tip asymptote for the crack width at each tip according to (76),

$$\Omega_n = \mathcal{W}(\zeta_n - \zeta_0, \dot{\gamma}), \quad \Omega_{N-n+1} = \mathcal{W}(\zeta_{N+1} - \zeta_{N-n+1}, \dot{\gamma}) \quad (91)$$

and by the global volume balance (37) discretized as

$$\mathcal{V}(\zeta_n - \zeta_0, \dot{\gamma}) + \mathcal{V}(\zeta_{N+1} - \zeta_{N-n+1}, \dot{\gamma}) + \sum_{i=n}^{N-n} \frac{\Delta\zeta_i}{2} (\Omega_i + \Omega_{i+1}) = \tau \quad (92)$$

Above, \mathcal{V} is the fluid volume stored in the tip region, computed according to (76):

$$\mathcal{V}(\zeta, \dot{\gamma}) = \int_0^{\zeta} \mathcal{W}(\eta, \dot{\gamma}) d\eta \quad (93)$$

The above equations form a closed system for the $3(N - 2n + 2) + 1$ unknowns. For a given crack length γ_M , the width basis functions $\omega_i^p(\zeta)$ (for $i = n : N - n + 1$ and $p = 0, 1$) and $\omega_i(\zeta)$ (for $i = 0, N + 1$) are first constructed from the XFEM solution for the elasticity problem (24)–(27) in which one of the boundary conditions (a)–(c) is imposed (see Section 4.2.1). An initial guess for the nodal quantities and the time-step is then chosen. These $3(N - 2n + 2) + 1$ nonlinear equations are solved iteratively using Newton’s algorithm until a predefined tolerance is reached.

5. Numerical results

5.1. $P \rightarrow W$ scheme: a crack parallel to a free surface with a fluid lag

We consider a partially fluid-filled hydraulic fracture propagating parallel to the free surface of a half-space. It is assumed that a large confining stress σ_ℓ is acting parallel to the free surface, and a confining stress $\hat{\sigma}_n = \sigma_o \ll \sigma_\ell$ acts normal to the crack plane. The large confinement σ_ℓ resists any symmetry-breaking curvature of the crack so that it continues to propagate parallel to the free surface [44]. The shear stress is zero along the crack faces, i.e., $\hat{\sigma}_s = 0$. Due to the reduced stress environment near the surface, the fluid front lags significantly behind the fracture front. To illustrate the performance of the coupled $P \rightarrow W$ scheme for this problem, we provide a comparison with the solution obtained using a displacement discontinuity method (DDM)-based algorithm Oribi [42,45].

We consider a crack at a depth H below the free surface, referring to the dimensionless coordinates (x, y) , in which the crack is located along $y = 0$, and the fluid inlet is at $x = y = 0$. To transition between the scaling used in the present paper and that used in Oribi, we represent the results in terms of the following scaled quantities, that take into account the characteristic length scale H :

$$T_* = H^{3/2}, \quad P_* = H^{-1/2}, \quad W_* = H^{1/2}, \quad L_* = H \quad (94)$$

so that

$$\tau = T_* \tau_*, \quad \Pi = P_* \Pi_*, \quad \Omega = W_* \Omega_*, \quad \gamma = L_* \gamma_*, \quad \gamma_f = L_* \gamma_{f*}, \\ \zeta = L_* \zeta_*$$

Note that the net scaled pressure Π_* accounts for the confining stress σ_o acting normal to the fracture plane while the scaled confining stress S_* is defined by

$$\sigma_o = P_* S_* \quad (95)$$

In the following two simulations, we used $\mathcal{K} = 0.5$ and either $S_* = 0$ or $S_* = 0.05$. The crack was initiated at depth $H = 45.5$ and constrained to grow parallel to the free surface. The size of the finite, rectangular computational domain was $L_x = 300$, $L_y = 125$, with singly- and doubly-infinite elements of order 9 placed along its three sides simulating the remote boundary. The mesh size was $h = 1$, and the initial crack half-length was set to $\gamma_0 \approx 19$, for which the solution initialized to the numerical solution obtained from Oribi. Fig. 4 shows a symmetric wing of the crack configuration after one step of the simulation and a fragment of the FEM mesh. The crack was propagated along its initial direction, with the crack extension on each wing of the crack being set to $\Delta\gamma = 1$. The fluid front tolerance was set to $\delta_f = 10^{-3}$, and the Picard iteration relaxation parameter for the fluid front velocity was set to $\chi = 0.8$ (for $S_* = 0$) and to $\chi = 0.9$ (for $S_* = 0.05$).

The crack tip region was dry during propagation within the time-frame chosen, so that the appropriate power-law exponent for the singular tip enrichment was $\lambda = 1/2$. The radius of the tip enrichment was set to $\rho = 3$. Fig. 5 shows the evolution of the scaled crack half-length γ_* , the fluid front γ_{f*} , the inlet crack width $\Omega_*(0, \tau_*)$ and the inlet net pressure $\Pi_*(0, \tau_*)$ with scaled time τ_* . A few snapshots of the scaled nodal crack widths and the nodal net pressures are shown in Fig. 6. All the results agree well with the Oribi solution.

In both simulations, the time-step was found by determining the root of the nonlinear function (68). We used the averaged propagation criterion (69) for the case when $S_* = 0$. We found, however, that the averaged propagation criterion (69) was not sufficiently accurate to obtain convergent results for the time-step when $S_* = 0.05$. We thus used the criterion in the form (70) for $S_* = 0.05$, in which we assumed that $\mathcal{K}_{II} = 0$, due to the large confining stress σ_ℓ acting parallel to the crack surface, and where the stress intensity factor \mathcal{K}_I was computed using the interaction integral as described in Appendix B. Indeed, the gradient of $f(\Delta\tau(\mathcal{K}))$ with respect to \mathcal{K} is typically very small, which implies that a very small error in \mathcal{K} will be associated with a large change in $\Delta\tau$. Thus a high degree of precision is required in the evaluation of \mathcal{K} in order that $\Delta\tau$ can be determined sufficiently accurately.

5.2. $P \rightarrow W$ scheme: a curving crack close to a free surface with a fluid lag

We consider a straight crack initially at a depth $H = 40.5$ below the free surface of a half-space in which there are no confining stresses, so that $\sigma_\ell = \sigma_o = 0$. The applied normal and shear tractions, in the absence of the crack, are therefore zero along the crack

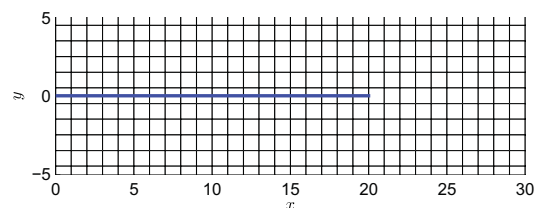


Fig. 4. A fragment of the FEM mesh and the crack configuration at the first step of the algorithm for the simulation with a flat partially-filled crack.

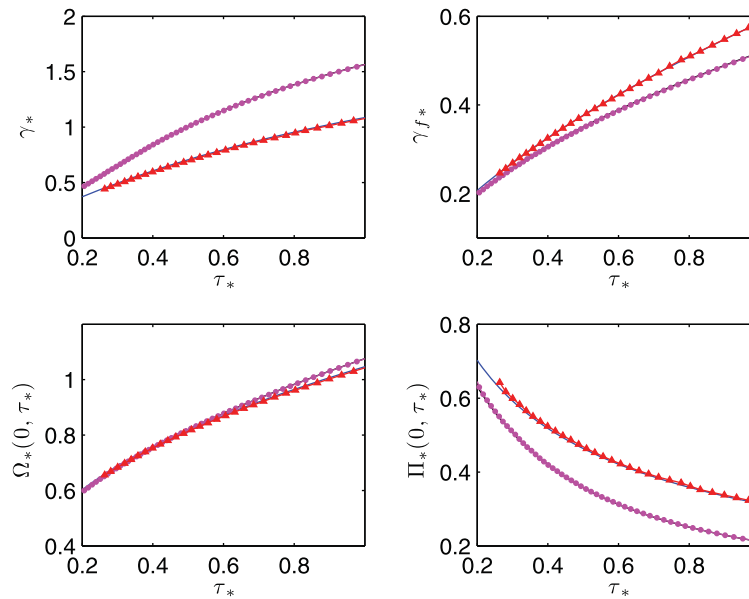


Fig. 5. Simulation results for $\mathcal{K} = 0.5$: evolution of the crack half-length γ_* , the fluid front $\gamma_{f,*}$, the inlet crack width $\Omega_*(0, \tau_*)$ and the inlet net pressure $\Pi_*(0, \tau_*)$. The results correspond to $S_* = 0$ (OriBi in black; XFEM in magenta with circles) and to $S_* = 0.05$ (OriBi in blue; XFEM in red with triangles). (For interpretation of the references to color in this figure legend, the reader is referred to the web version of this article.)

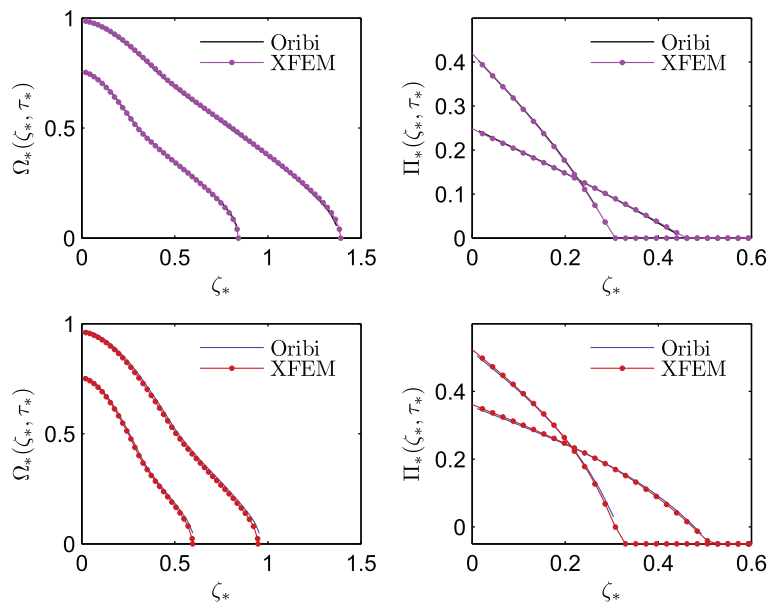


Fig. 6. Simulation results for $\mathcal{K} = 0.5$: crack width and net pressure at times $\tau_* \approx 0.4, 0.8$. The results correspond to $S_* = 0$ (top: OriBi in black; XFEM in magenta with circles) and to $S_* = 0.05$ (bottom: OriBi in blue; XFEM in red with circles). (For interpretation of the references to color in this figure legend, the reader is referred to the web version of this article.)

path, $\hat{\sigma}_n = \hat{\sigma}_s = 0$. In this case the propagating fracture curves towards the free surface. The crack is partially filled with fluid for the duration of the simulation, and as it propagates towards the surface, the two moving boundaries γ and γ_f , as well as the shape of the fracture, need to be determined. The results of the coupled $P \rightarrow W$ scheme for this problem are compared to the results of OriBiC, an extension of OriBi designed to treat curved cracks based on the maximum tensile stress criterion (70) [40,41].

The dimensionless toughness is set to $\mathcal{K} = 0.5$. We refer again to the dimensionless coordinates (x, y) , in which the initial crack is located along $y = 0$, and the fluid inlet is located at $x = y = 0$. In the XFEM simulation for this example, the size of the finite, rectangular computational domain was $L_x = 300$, $L_y = 121$, with singly- and

doubly-infinite elements of order 9 placed along its three sides to simulate the remote boundary. The mesh size was $h = 1$, and the initial crack half-length was set to $\gamma_0 = 18$ and the XFEM solution was initialized to the corresponding numerical solution from OriBiC. Further crack propagation was modeled by adding straight segments to the crack tips extending over two finite elements, so that the crack kinks were only present at edges of the finite element mesh, and the crack path was straight within each particular element cut by the crack. The deflection angle of each new segment was determined from the stress intensity factors via (71). The power-law exponent for the singular tip enrichment was $\lambda = 1/2$. The tip enrichment was introduced only for finite elements that contained the crack tip along one of its edges. The fluid front toler-

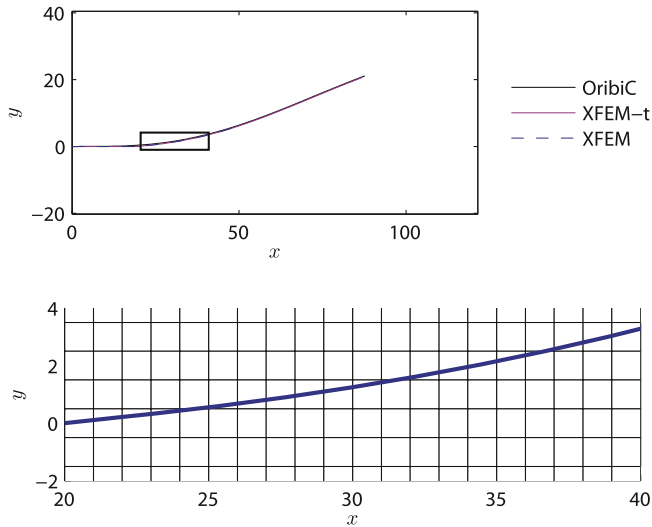


Fig. 7. Top: the crack path obtained using OriBiC, XFEM-t, and XFEM; bottom: a fragment of the crack path within the FEM mesh sampled within the rectangular box shown in the top figure.

ance was set to $\delta_f = 10^{-3}$, and the Picard iteration relaxation parameter for the fluid front velocity was set to $\chi = 0.9$. The resulting crack path obtained using the XFEM is shown in Fig. 7, together with a fragment of the underlying FEM mesh that covers the rectangular box shown in the upper figure. The results show close agreement to those obtained using OriBiC.

Fig. 8 shows the evolution of the scaled crack half-length γ_* , the fluid front γ_{f*} , the inlet crack width $\Omega_*(0, \tau_*)$, and the inlet pressure $\Pi_*(0, \tau_*)$ with the scaled time τ_* . A few snapshots of the scaled nodal crack widths and the nodal pressures are also shown. The same scaling introduced in (94) is used.

In the simulation, the criterion (70) was used to find the time-step. However, this leads to instability in the XFEM solution around $\tau_* = 0.5$, as can be seen from Fig. 8. It was found that the computation of the stress intensity factors for a kinking crack, which is sufficiently accurate to determine the deflection angle of the crack path, is not accurate enough to determine the time-step using (68) combined with (70). The sensitivity of the time-step selection to errors in the stress intensity factor \mathcal{K} was noted in the previous example. It should be noted that using line segments to approximate a curving crack introduces mechanical artifacts, in the form of kinks, into the numerical model. The resolution to this would be to use C^1 curvilinear crack segments with the appropriate tangent asymptotics at the tips. However, this line of investigation is beyond the scope of this paper. To demonstrate that this instability is solely due to the time-step selection procedure, we performed a simulation for the same set of parameters within the coupled XFEM, but enforced the time-step given by the OriBiC solution at each crack configuration. The results of this simulation are shown in Figs. 7 and 8, denoted by “XFEM-t”. We note that the results of the original coupled XFEM (for $\tau_* < 0.5$) and of the simulation with the time-step enforced are both in good agreement with each other and with OriBiC. It should be noted that the number of mesh points along the crack in the XFEM model were an order of magnitude (110 per crack wing) less than those used in the OriBiC model (920 per crack wing). This example does demonstrate, however,

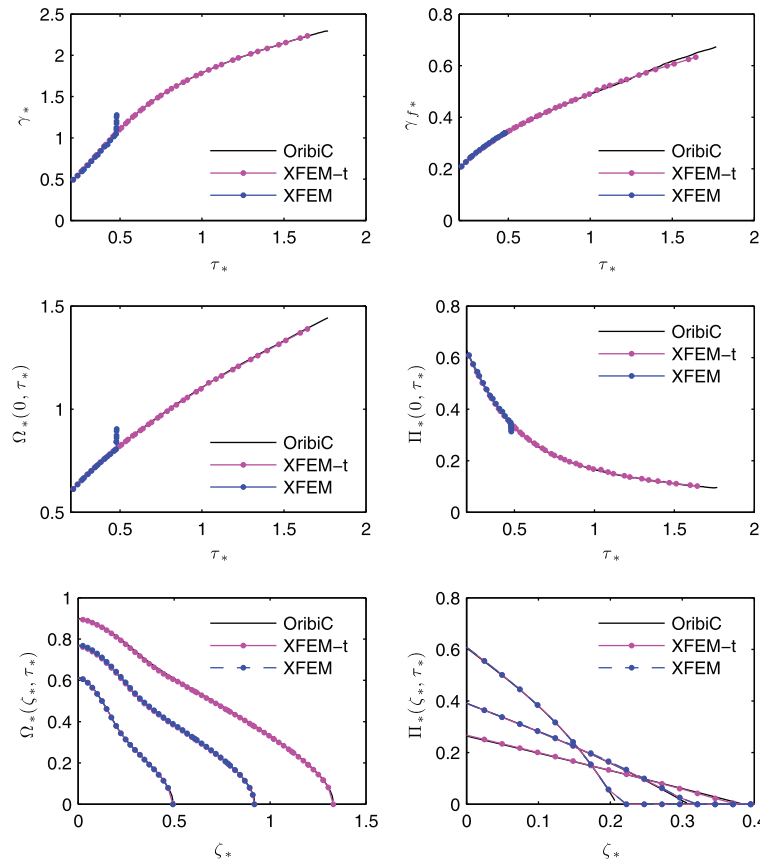


Fig. 8. Simulation results for a curving partially-filled crack with $\mathcal{K} = 0.5$. Plots show the evolution of: the crack half-length γ_* , the fluid front γ_{f*} , the inlet crack width $\Omega_*(0, \tau_*)$, and the inlet pressure $\Pi_*(0, \tau_*)$. Spatial plots of the crack width and pressure at times $\tau_* \approx 0.2, 0.4, 0.6$ are also shown. (OriBiC in black; XFEM-t in magenta with circles; XFEM blue with circles). (For interpretation of the references to color in this figure legend, the reader is referred to the web version of this article.)

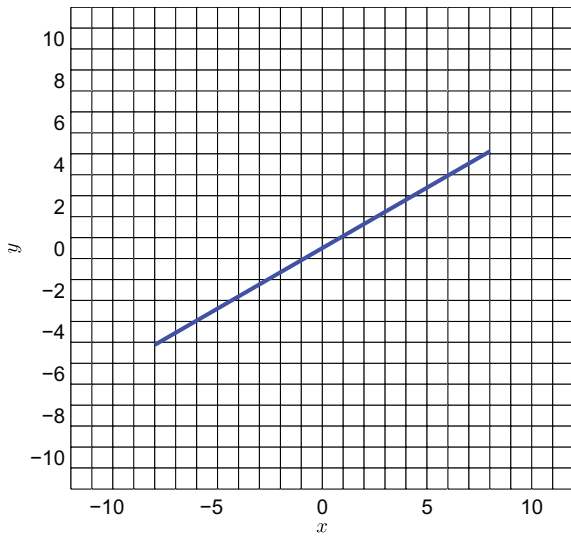


Fig. 9. A fragment of the FEM mesh and the initial crack configuration.

that the XFEM-based $P \rightarrow W$ scheme does provide a sufficiently accurate representation of the elasticity problem to resolve this challenging problem of a curving hydraulic fracture to capture the significant geometric changes that take place during the propagation. We leave the exploration of more robust time-step selection techniques or alternative front location methods to a subsequent paper.

5.3. P&W scheme: M-vertex solution

We use the coupled P&W scheme to model the propagation of a hydraulic fracture in an infinite domain corresponding to the M-vertex solution, characterized by $\mathcal{K} = 0$ and zero lag. We use the viscosity scaling that leads to the power law relationships (23). To provide a comparison between the XFEM algorithm and the reference M-vertex solution [46,16] for the more challenging situation in which the crack is not aligned with the structured mesh, we modeled a crack inclined at 30° to the x -axis, in a rectangular domain of dimensions $L_x = 240$, $L_y = 241$, with singly- and doubly-infinite elements of order 9 placed along its four sides to simulate the infinite domain. The mesh size was $h = 1$, and the initial crack half-length was set to $\gamma_0 = 9.5$, for which the solution was initialized to the M-vertex solution. Fig. 9 shows the initial crack configuration and a fragment of the FEM mesh that was used. The crack was then propagated along its initial direction for 60 steps, with the crack extension on each wing of the crack being set to $\Delta\gamma = 1$. The asymptotic tip region at each step was chosen to spread over two elements for each crack tip; this corresponds to setting $n = 2$ in the P&W scheme.

The propagation condition in this problem corresponds to the viscosity tip width asymptote (35), so that the power-law exponent for the singular tip enrichment was set to $\lambda = 2/3$. The radius of the tip enrichment was set to $\rho = 3$.

Fig. 10 shows the evolution of the crack half-length γ , the fluid volume $\int_{-\gamma}^{\gamma} \Omega d\zeta$, the inlet crack width $\Omega(0, \tau)$ and the inlet fluid pressure $\Pi(0, \tau)$ with time τ . A few snapshots of the nodal crack widths and the nodal fluid pressures are shown in Fig. 11. All the results agree well with the M-vertex solution. For this comparison,

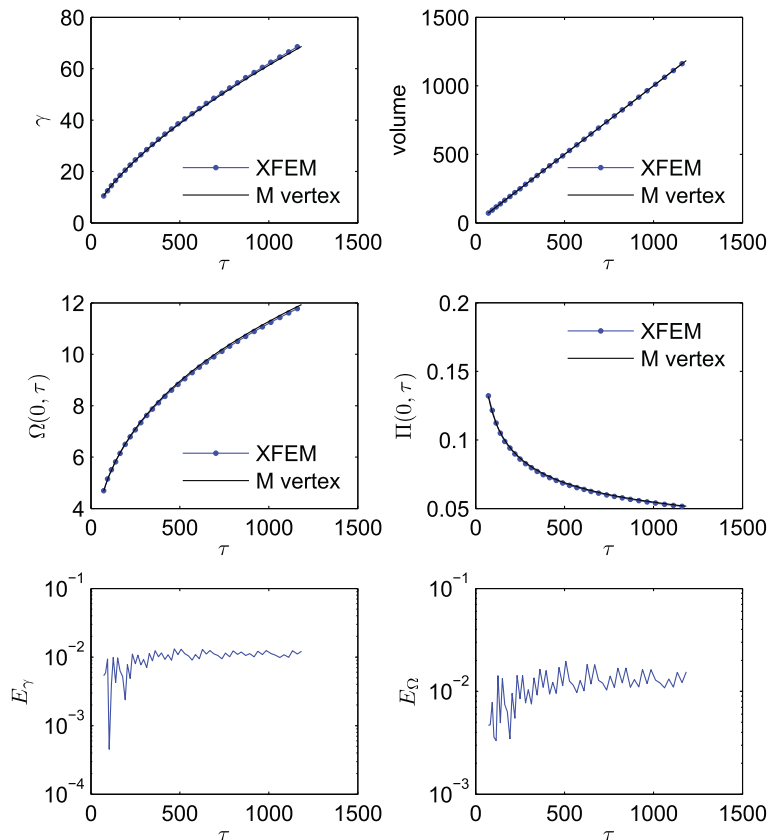


Fig. 10. Simulation results for $\mathcal{K} = 0$: evolution of crack half-length γ , fluid volume $\int_{-\gamma}^{\gamma} \Omega d\zeta$, inlet crack width $\Omega(0, \tau)$, inlet fluid pressure $\Pi(0, \tau)$; and the relative errors in length and width. These plots show the dimensionless quantities defined in (17) and (18) (M vertex in black and XFEM in blue with circles). (For interpretation of the references to color in this figure legend, the reader is referred to the web version of this article.)

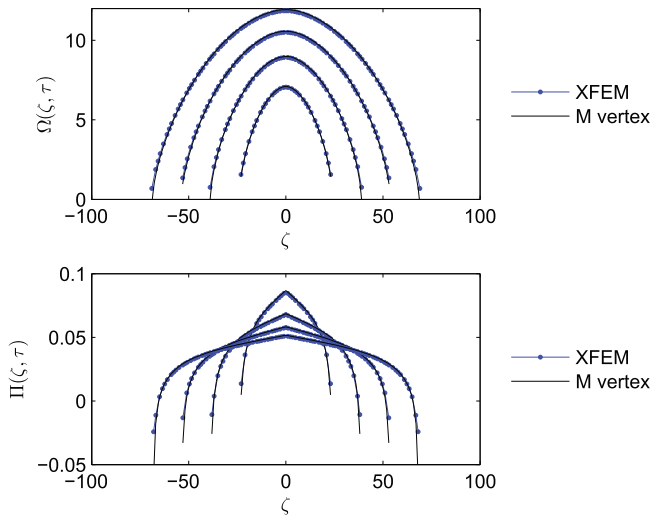


Fig. 11. Simulation results for $\mathcal{K}=0$: crack width and fluid pressure at times $\tau \approx 249, 507, 824, 1184$ (M vertex in black and XFEM in blue with circles). (For interpretation of the references to color in this figure legend, the reader is referred to the web version of this article.)

we define the relative approximation errors in length and width at each time-step as follows:

$$E_\gamma(\tau) = \frac{|\gamma(\tau) - \gamma^{ref}(\tau)|}{\gamma^{ref}(\tau)}, \quad E_\Omega(\tau) = \sqrt{\frac{\sum_{i=1}^N (\Omega_i - \Omega_i^{ref})^2}{\sum_{i=1}^N (\Omega_i^{ref})^2}} \quad (96)$$

where the superscript *ref* denotes the quantities corresponding to the M-vertex solution at time τ . Note that the above definition of the width error $E_\Omega(\tau)$, based on the nodal crack widths, can be viewed as a discrete version of the L_2 -norm of the error, scaled by the L_2 -norm of the reference solution:

$$E_\Omega(\tau) \sim \frac{\|\Omega - \Omega^{ref}\|_{L_2(\Sigma)}}{\|\Omega^{ref}\|_{L_2(\Sigma)}}$$

The evolution of the relative approximation errors in length and width, $E_\gamma(\tau)$ and $E_\Omega(\tau)$, are shown in Fig. 10. It is observed that these errors essentially asymptote to 10^{-2} and do not grow with time. These errors are not related to the approximation of the domain by the infinite elements since they do not grow as the crack tips approach the Finite Element–Infinite Element Interface. These results also confirm that the XFEM formulation used in the P&W scheme is mesh-independent.

6. Conclusions

Hitherto, there has been little research on XFEM-based schemes to couple the elasto-hydrodynamic equations that govern the propagation of hydraulic fractures. Indeed, previous research in this area focused on so-called dry cracks, in which the effect of viscosity can essentially be neglected. These schemes exploit the $O(h^2)$ ND map provided by the XFEM. We have demonstrated that it is also possible to exploit the $O(h^2)$ ND map even if viscous effects are significant. In particular, if there is a finite fluid lag, so that the pressure field is finite, then the so-called $P \rightarrow W$ XFEM formulation based on inverting the ND map and using $\lambda = \frac{1}{2}$ enrichment, is sufficient to capture the HF solution with the required precision. However, if there is a coalescence of the fluid and fracture fronts, which frequently occurs in typical HF treatments in deep reservoirs, then the degenerate lubrication PDE admits singular behavior of the pressure field in the fracture tips. Unfortunately, the singularity of

this pressure field and the fact that the domain of validity of the tip pressure asymptotic solution is extremely small $\lesssim 1\%$ compared to the length of the fracture, makes it impracticable to use the ND map approach, in which the singular asymptotic tip pressure field is combined with polynomial basis functions away from the tips. By contrast, the domain of validity of the asymptotic solution for the width field extends farther from the fracture tip, covering up to $\sim 10\%$ of the fracture. This larger domain of validity of the tip width asymptotic solution makes it natural to consider a scheme based on the DN map. In this scheme, the tip width asymptotes are combined with polynomial basis functions to represent the width field away from the tips. However, we have found that this does not lead to a successful scheme due to the poor $O(h)$ XFEM convergence rate when resolving the DN map and the errors in the pressure field due to parasitic modes introduced by the blending between the enriched region near the tips and the remainder of the fracture when solving the DN map. Therefore, for this class of problem, in which the tip pressure field is singular, we have developed the novel P&W XFEM scheme. Similar to the decomposition in [24], the fracture is logically divided into tip regions and a channel region. Within the tip regions it is assumed that the width field is given by the asymptotic solution, while in the channel region the fluid-flow equations are used to define the pressure field and the XFEM uses the $O(h^2)$ ND map to determine the corresponding widths in the channel region. At the interfaces between the tip and channel regions, boundary conditions are prescribed that are consistent with the tip asymptotes. Typically, for these singular pressure fields, the index λ of the power law for the tip width field is greater than $\frac{1}{2}$, so that non-standard enrichment basis functions are required.

These two distinct XFEM formulations are able to deal with the full range of complex behavior typically encountered when modeling propagating HF – even those with singular pressure fields. HF propagation typically also involves multiple length scales (sometimes differing by 8 orders of magnitude) as each of the multiple competing physical processes manifest themselves at different characteristic lengths. The P&W XFEM scheme can also be used in this situation by matching to an asymptotic solution that applies at the computational length scale and which captures the behavior of the HF at finer length scales. In all the simulations, the free boundary was located by assuming a growth increment $\Delta\gamma$ in a particular growth direction and the free boundary was identified in space–time by determining the corresponding time step $\Delta\tau$.

In the numerical examples provided we consider three test problems. The first two problems involved HF propagating with a finite fluid lag due to the presence of a free surface. In both cases the HF is assumed to initiate parallel to the free surface. In the first of these fluid-lag problems, the HF was constrained to propagate parallel to the free surface. The $P \rightarrow W$ XFEM algorithm performs well for this problem and yields results that agree well with the solution obtained from another numerical algorithm Oribi, which is based on a DDM. In the second fluid-lag problem, the high confinement perpendicular to the free surface is relaxed so that the fracture curves toward the free surface due to the reduction in confining stress. The $P \rightarrow W$ XFEM solution captures shape of the curving fracture and generates pressure and width fields all of which agree well with the DDM-based OribiC comparison solution. This example highlights the limitation of the time-step approach to locating the free boundary, due to the sensitivity of the time-step selection to errors in the stress intensity factor \mathcal{K} . The third example involves a viscosity-driven HF propagating in an infinite homogeneous elastic medium, for which the M-vertex solution [27,16] is used to assess the accuracy of the XFEM. In this case the fluid and fracture fronts coalesce resulting in a pressure field that is singular at the fracture tips. It is thus necessary to use the P&W XFEM formulation, which yields a solution that shows close agreement with

the M-vertex solution in spite of the fact that the crack in the XFEM model was deliberately constrained to grow along a line that is inclined at an angle of 30° to the x-axis so that it is not aligned with the structured FEM mesh. The relative errors in the fracture length γ and the fracture widths Ω asymptote to approximately 1%.

Acknowledgements

The MATLAB codes used for numerical simulations in this paper were based on the original MATLAB software package for XFEM implementation in a domain with a crack by Dr.-Ing. T.-P. Fries (RWTH Aachen University), available at www.xfem.rwth-aachen.de/Background/Download/XFEM_Download.php. The authors gratefully acknowledge this resource. This work was partially funded by the NSERC Discovery Grants program, which both authors gratefully acknowledge.

Appendix A. Interaction integral for SIF computation

The stress intensity factors (SIFs) for the simulation results presented in Section 5.2 were computed using a domain form of the interaction integral (see [47–52]). We consider a 2D plane strain problem with a curved crack, using a 2D version of the interaction integral formulation proposed by Gosz and Moran [52] for 3D non-planar cracks. We consider the crack tip neighborhood domain \tilde{V} illustrated in Fig. 12, which contains a part of the curved crack surface Σ . The crack surface asymptotes to a fictitious straight line crack C tangent to the actual crack immediately at its tip. In the numerical implementation the curves Σ and C intersect over a finite segment \hat{C} , while $\tilde{\Sigma}$ and \tilde{C} denote the non-intersecting portions of the curves Σ and C within the domain \tilde{V} . The boundary of \tilde{V} is then represented by $\partial\tilde{V} = \tilde{C}^+ \cup \hat{C}^+ \cup \hat{C}^- \cup \tilde{\Sigma}^- \cup \Gamma_o$ (see Fig. 12(a)).

The mode I and II SIFs are found from the interaction integral I^m , corresponding to mode $m = I, II$:

$$K_m = \frac{E'}{2} I^m, \quad m = I, II \tag{97}$$

and computed from:

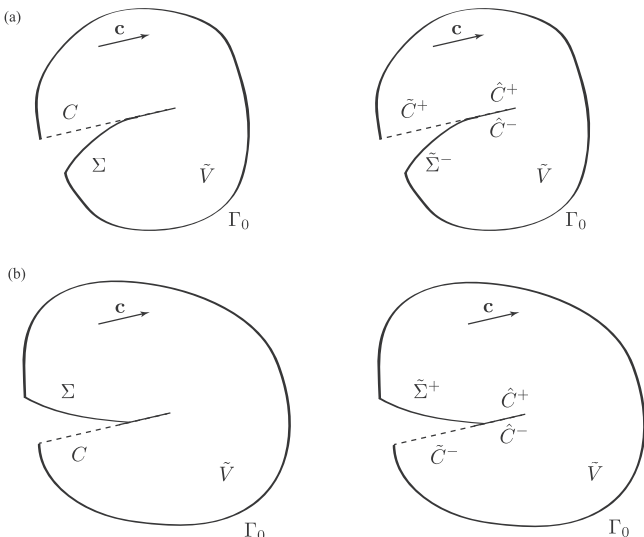


Fig. 12. Regions for interaction integral: (a) neighborhood domain \tilde{V} containing the Σ^- branch of the crack surface Σ and (b) neighborhood domain \tilde{V} containing the Σ^+ branch of the crack surface Σ .

$$I^m = - \int_{\tilde{V}} c_i \alpha_j P_{ij}^m dV - \int_{\tilde{C}^+ \cup \hat{C}^+ \cup \hat{C}^-} \alpha c_i U_{,i}^m S_{ij} n_j dC + \int_{\tilde{\Sigma}^-} \alpha c_i P_{ij}^m n_j d\Sigma \tag{98}$$

where $P_{ij}^m = S_{ik} E_{kj}^m \delta_{ij} - U_{,i}^m S_{ij} - U_{,i} S_{ij}^m$, and the superscript m denotes the elastic fields corresponding to the (auxiliary) asymptotic mode I (with $K_I = 1$) and mode II (with $K_{II} = 1$) plane strain solutions, respectively. In (98), n_j are components of the outward unit normal vector along each integration path involved; c_j are components of the vector \mathbf{c} tangent to the fictitious crack (see Fig. 12), and $\alpha(\mathbf{x})$ is a smooth function such that $\alpha = 1$ at the crack tip and $\alpha = 0$ along the path Γ_o . Tensors U_i , S_{ij} and E_{ij} above denote the components of the displacement, stress and strain, respectively. When the actual and fictitious cracks are oriented as shown in Fig. 12(b), the two path integrals in (98) are taken over $\tilde{C}^- \cup \hat{C}^- \cup \hat{C}^+$ and $\tilde{\Sigma}^+$, respectively. Expression (98) for the interaction integral makes it possible to account for non-zero tractions along a curved crack path. In adapting the general form of the interaction integral [52] to a plane strain problem, we assume that the auxiliary solutions satisfy equilibrium and compatibility equations and that the tractions associated with these solutions along the fictitious crack C are zero. These assumptions are fulfilled by the asymptotic mode I and II elastic fields.

Appendix B. Infinite elements

For the numerical examples in this paper, we consider a finite rectangular domain V that is mapped onto an infinite domain \tilde{V} . The finite domain V is discretized into a regular rectangular mesh of elements. The elements in the interior of V , that are away from the crack, are standard isoparametric bilinear Lagrange elements. The elements along the external boundary Γ of V are subparametric singly infinite and doubly infinite elements constructed as described by Bettess [39].

Singly infinite element

To illustrate the infinite element construction, we consider a rectangular element defined by its four nodes (x_i, y_i) , $i = 1, \dots, 4$, such that its edges are aligned with the (x, y) axes (Fig. 13a). The mapping is based on the use of the following functions defined in terms of the reference coordinate $\xi \in [-1, 1]$:

$$M_1(\xi) = \frac{-2\xi}{1-\xi}, \quad M_2(\xi) = \frac{1+\xi}{1-\xi} \tag{99}$$

We also consider linear Lagrange functions,

$$L_1(\xi) = \frac{1-\xi}{2}, \quad L_2(\xi) = \frac{1+\xi}{2} \tag{100}$$

To map the nodes of the parent element corresponding to $\xi = 1$ to infinity, we use the mapping of the form [38,39,53]

$$x(\xi, \eta) = \mathbf{M}(\xi, \eta) \bar{\mathbf{X}}, \quad y(\xi, \eta) = \mathbf{M}(\xi, \eta) \bar{\mathbf{Y}} \tag{101}$$

where $(\xi, \eta) \in [-1, 1] \times [-1, 1]$ are the reference coordinates, and

$$\mathbf{M} = [M_1(\xi)L_1(\eta), M_2(\xi)L_1(\eta), M_2(\xi)L_2(\eta), M_1(\xi)L_2(\eta)]$$

$$\bar{\mathbf{X}} = [x_1, 2x_1, 2x_4, x_4]^T, \quad \bar{\mathbf{Y}} = [y_1, y_2, y_3, y_4]^T$$

This maps the parent finite element into a strip that is infinite in positive x direction (Fig. 13(c)).

The displacement field $\mathbf{u}(\xi, \eta)$ in the reference element is represented as a product of a linear function in η and a polynomial of order m in ξ . For this, a set of $(m + 1)$ nodes ξ_i is used in ξ -direction, and two nodes η_j are used in η -direction. The corresponding

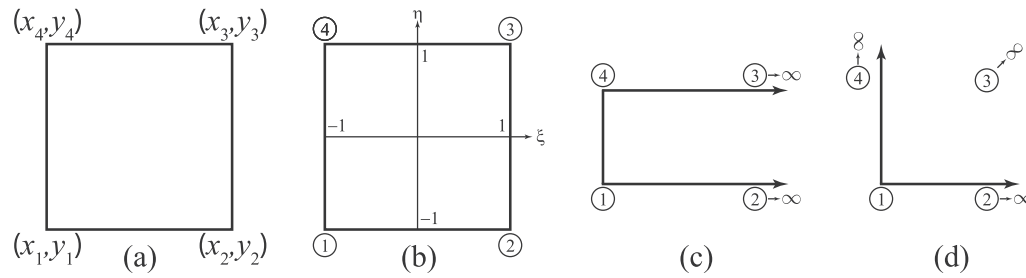


Fig. 13. Construction of infinite elements: (a) a rectangular finite element with (x, y) coordinates; (b) the reference element in (ξ, η) space; (c) a mapped singly infinite element in (x, y) space, and (d) a mapped doubly infinite element in (x, y) space.

shape functions comprise the products of the one-dimensional Lagrange polynomials $L_i^m(\xi)$ of order m and the one-dimensional linear Lagrange polynomials $L_j(\eta)$:

$$\mathbf{u}(\xi, \eta) = \sum_{i=1}^m \sum_{j=1}^2 \mathbf{u}(\xi_i, \eta_j) L_i^m(\xi) L_j(\eta)$$

This representation makes it possible to express the displacement field in terms of a product of a linear function of y , and a polynomial in x^{-1} of order m , providing an approximation to the decay behavior in powers of x^{-1} as $x \rightarrow +\infty$. When $m > 2$, this infinite element is subparametric [39], in that a lower-order representation is used for the mapping functions than that used for the displacement shape functions.

Doubly infinite element

A corner element of the quadrilateral mesh is mapped onto a doubly infinite element [38,39] to represent the decaying asymptotic behavior of the displacement field as $x, y \rightarrow +\infty$ (Fig. 13(d)). To map the nodes of the parent finite element corresponding to either $\xi = 1$ or $\eta = 1$, to infinity, the mapping has the form (101) with

$$\mathbf{M} = [M_1(\xi)M_1(\eta), M_2(\xi)M_1(\eta), M_2(\xi)M_2(\eta), M_1(\xi)M_2(\eta)]$$

$$\bar{\mathbf{X}} = [x_1, 2x_1, 2x_4, x_4]^T, \quad \bar{\mathbf{Y}} = [y_1, y_2, 2y_1, 2y_2]^T$$

This maps the parent finite element into a quarter-plane that is infinite in positive x and y directions.

The displacement field $\mathbf{u}(\xi, \eta)$ in the reference element is represented as a product of polynomials of order m in both ξ and η . Thus, $(m+1)$ nodes ξ_i are used in ξ -direction, and $(m+1)$ nodes η_j are used in η -direction. The corresponding shape functions comprise the products of the one-dimensional Lagrange polynomials of order m :

$$\mathbf{u}(\xi, \eta) = \sum_{i=1}^m \sum_{j=1}^m \mathbf{u}(\xi_i, \eta_j) L_i^m(\xi) L_j^m(\eta)$$

The displacement field is thus expressed in terms of a product of polynomials in x^{-1} and y^{-1} of order m , representing the decay of the displacement field as $x, y \rightarrow +\infty$. Again, this infinite element is subparametric for $m > 2$ [39].

Discussion

As described above, singly and double infinite elements are constructed along the sides and at the corners of the rectangular finite domain V . Due to the use of the regular quadrilateral mesh and the mapping (101), which represents the coordinates via $x = x(\xi)$ and $y = y(\eta)$, the integrals required in the assembly of the stiffness matrix from the infinite elements involve products of polynomials of the reference coordinates ξ and η . Thus Gauss–Legendre quadra-

ture rules of sufficient order applied to these integrals in the reference domain are exact.

For a horizontal crack of half-length γ in an infinite domain, we found that to guarantee that the relative error in the interpolated crack width due to approximation of the infinite domain by infinite elements does not exceed 10^{-2} , it is sufficient to use infinite elements of order 9, in the rectangular domain of dimensions $L_x \times L_y$, where $\gamma \approx L_y/2 \approx L_x/4$ and where the crack is located in the center of the domain. This was used as a guideline for choosing the size of the domain in all numerical examples in this work.

Appendix C. Hermite cubic polynomials

The following are the expressions for Hermite cubic basis functions:

$$H_i^0(\zeta) = \begin{cases} \frac{[\Delta\zeta_{i-1} + 2(\zeta_i - \zeta)](\zeta - \zeta_{i-1})^2}{(\Delta\zeta_{i-1})^3}, & \text{if } \zeta_{i-1} \leq \zeta < \zeta_i \\ \frac{[\Delta\zeta_i + 2(\zeta - \zeta_i)](\zeta_{i+1} - \zeta)^2}{(\Delta\zeta_i)^3}, & \text{if } \zeta_i \leq \zeta < \zeta_{i+1} \\ 0, & \text{else} \end{cases}$$

$$H_i^1(\zeta) = \begin{cases} \frac{(\zeta - \zeta_i)(\zeta - \zeta_{i-1})^2}{(\Delta\zeta_{i-1})^2}, & \text{if } \zeta_{i-1} \leq \zeta < \zeta_i \\ \frac{(\zeta - \zeta_i)(\zeta_{i+1} - \zeta)^2}{(\Delta\zeta_i)^2}, & \text{if } \zeta_i \leq \zeta < \zeta_{i+1} \\ 0, & \text{else} \end{cases}$$

where $\Delta\zeta_i = \zeta_{i+1} - \zeta_i$.

References

- [1] R. Jeffrey, K. Mills, Hydraulic fracturing applied to inducing longwall coal mine goaf falls, in: Pacific Rocks 2000, Balkema, Rotterdam, 2000, pp. 423–430.
- [2] A. van As, R. Jeffrey, Caving induced by hydraulic fracturing at Northparkes mines, in: Pacific Rocks 2000, Balkema, Rotterdam, 2000, pp. 353–360.
- [3] P. Valkó, M. Economides, Hydraulic Fracture Mechanics, John Wiley & Sons, Chichester, UK, 1995.
- [4] M. Economides, K. Nolte (Eds.), Reservoir Stimulation, third ed., John Wiley & Sons, Chichester, UK, 2000.
- [5] U. Frank, N. Barkley, Remediation of low permeability subsurface formations by fracturing enhancements of soil vapor extraction, J. Hazard. Mater. 40 (2005) 191–201.
- [6] L. Murdoch, Mechanical analysis of idealized shallow hydraulic fracture, J. Geotech. Geoenviron. 128 (6) (2002) 488–495.
- [7] A.R. Ingraffea, T.J. Boone, D.V. Swenson, Computer Simulation of Fracture Processes, 1991 (Chapter 12).
- [8] K. Shah, B. Carter, A. Ingraffea, Hydraulic fracturing simulation in parallel computing environments, Int. J. Rock Mech. Min. Sci. 34 (3/4) (1997) 474.
- [9] N. Moës, J. Dolbow, T. Belytschko, A finite element method for crack growth without remeshing, Int. J. Numer. Methods Eng. 46 (1999) 131–150.
- [10] M. Stolarska, D. Chopp, N. Moës, T. Belytschko, Modeling crack growth by level sets and the extended finite element method, Int. J. Numer. Methods Eng. 51 (2001) 943–960.
- [11] N. Sukumar, J. Prevost, Modeling quasi-static crack growth with the extended finite element method part i: computer implementation, Int. J. Solids Struct. 40 (2002) 7513–7537.
- [12] A. Taleghani, Analysis of hydraulic fracture propagation in fractured reservoirs: an improved model for the interaction between induced and

- natural fractures, Ph.D. Thesis, The University of Texas at Austin, The University of Texas at Austin, May 2009.
- [13] Q.-W. Ren, Y.-W. Dong, T.T. Yu, Numerical modeling of concrete hydraulic fracturing with extended finite element method, *Sci. China Ser. E: Technol. Sci.* 52 (2009) 559–565.
- [14] B. Lecampion, An extended finite element method for hydraulic fracture problems, *Commun. Numer. Methods Eng.* 25 (2009) 121–133.
- [15] J. Desroches, E. Detournay, B. Lenoach, P. Papanastasiou, J. Pearson, M. Thiercelin, A.-D. Cheng, The crack tip region in hydraulic fracturing, *Proc. R. Soc. London, Ser. A* 447 (1994) 39–48.
- [16] J. Adachi, E. Detournay, Self-similar solution of a plane-strain fracture driven by a power-law fluid, *Int. J. Numer. Anal. Methods Geomech.* 26 (2002) 579–604.
- [17] J. Adachi, E. Detournay, Plane-strain propagation of a fluid-driven fracture: finite toughness self-similar solution, *Int. J. Solids Struct.*, in preparation.
- [18] S.L. Mitchell, R. Kuske, A.P. Peirce, An asymptotic framework for the analysis of hydraulic fractures: the impermeable case, *ASME J. Appl. Mech.* 74 (2) (2007) 365–372.
- [19] J. Adachi, E. Detournay, Plane strain propagation of a hydraulic fracture in a permeable rock, *Eng. Fract. Mech.* 75 (16) (2008) 4666–4694.
- [20] D. Garagash, E. Detournay, J. Adachi, Multiscale Tip Asymptotics in Hydraulic Fracture with Leak-off, *J. Fluid Mech.* 669 (2011) 260–297.
- [21] A. Savitski, E. Detournay, Propagation of a fluid-driven penny-shaped fracture in an impermeable rock: asymptotic solutions, *Int. J. Solids Struct.* 39 (26) (2002) 6311–6337.
- [22] A. Bunger, E. Detournay, Asymptotic solution for a penny-shaped near-surface hydraulic fracture, *Eng. Fract. Mech.* 72 (16) (2005) 2468–2486.
- [23] A. Bunger, E. Detournay, Early time solution for a penny-shaped hydraulic fracture, *ASCE J. Eng. Mech.* 133 (5) (2007) 534–540.
- [24] A.P. Peirce, E. Detournay, An implicit level set method for modeling hydraulically driven fractures, *Comput. Methods Appl. Mech. Eng.* 197 (2008) 2858–2885, <http://dx.doi.org/10.1016/j.cma.2008.01.013>.
- [25] S.L. Mitchell, R. Kuske, A. Peirce, An asymptotic framework for finite hydraulic fractures including leak-off, *SIAM J. Appl. Math.* 67 (2) (2007) 364–386.
- [26] E. Gordeliy, A.P. Peirce, D. Schötzau, Enrichment and convergence of the XFEM for hydraulic fracture problems, in preparation.
- [27] R. Carbonell, J. Desroches, E. Detournay, A comparison between a semi-analytical and a numerical solution of a two-dimensional hydraulic fracture, *Int. J. Solids Struct.* 36 (31–32) (1999) 4869–4888.
- [28] D. Garagash, Hydraulic fracture propagation in elastic rock with large toughness, in: J. Girard, M. Liebman, C. Breeds, T. Doe (Eds.), *Rock Around the Rim – Proc. 4th North American Rock Mechanics Symp.*, Balkema, Rotterdam, 2000, pp. 221–228, pdf.
- [29] D. Garagash, Plane-strain propagation of a fluid-driven fracture during injection and shut-in: asymptotics of large toughness, *Eng. Fract. Mech.* 73 (4) (2006) 456–481, <http://dx.doi.org/10.1016/j.engfracmech.2005.07.012>.
- [30] J. Rice, Mathematical analysis in the mechanics of fracture, in: H. Liebowitz (Ed.), *Fracture, an Advanced Treatise*, vol. II, Academic Press, New York, NY, 1968, pp. 191–311 (Chapter 3).
- [31] E. Detournay, Propagation regimes of fluid-driven fractures in impermeable rocks, *Int. J. Geomech.* 4 (1) (2004) 1–11.
- [32] A.P. Peirce, A Hermite cubic collocation scheme for plane strain hydraulic fractures, *Comput. Methods Appl. Mech. Eng.* 199 (29–32) (2010) 1949–1962, <http://dx.doi.org/10.1016/j.cma.2010.02.009>.
- [33] T.-P. Fries, A corrected XFEM approximation without problems in blending element, *Int. J. Numer. Methods Eng.* 75 (2008) 503–532.
- [34] G. Ventura, R. Gracie, T. Belytschko, Fast integration and weight function blending in the extended finite element method, *Int. J. Numer. Methods Eng.* 77 (2009) 1–29.
- [35] I. Babuska, J.M. Melenk, The partition of unity method, *Int. J. Numer. Methods Eng.* 40 (1997) 727–758.
- [36] P. Laborde, J. Pommier, Y. Renard, M. Salaün, High-order extended finite element method for cracked domains, *Int. J. Numer. Methods Eng.* 64 (2005) 354–381.
- [37] A. Zilian, T.-P. Fries, A localized mixed-hybrid method for imposing interfacial constraints in the extended finite element method (XFEM), *Int. J. Numer. Methods Eng.* 79 (2009) 733–752.
- [38] J. Marques, D. Owen, Infinite elements in quasi-static materially nonlinear problems, *Comput. Struct.* 18 (4) (1984) 739–751.
- [39] P. Bettess, *Infinite Elements*, Penshaw Press, 1992.
- [40] E. Gordeliy, E. Detournay, Numerical simulations of near-surface bowl-shaped hydraulic fractures, in preparation.
- [41] A. Bunger, E. Gordeliy, E. Detournay, Comparison between laboratory experiments and coupled simulations of saucer-shaped hydraulic fractures in homogeneous brittle-elastic solids, *J. Mech. Phys. Solids*, submitted for publication.
- [42] E. Gordeliy, E. Detournay, A fixed grid algorithm for simulating the propagation of a shallow hydraulic fracture with a fluid lag, *Int. J. Numer. Anal. Methods Geomech.* 35 (2011) 602–629.
- [43] F. Erdogan, G.C. Sih, On the crack extension in plates under plate loading and transverse shear, *J. Basic Eng.* 85 (1963) 519–527.
- [44] X. Zhang, E. Detournay, R. Jeffrey, Propagation of a penny-shaped hydraulic fracture parallel to the free-surface on an elastic half-space, *Int. J. Fract.* 115 (2002) 125–158.
- [45] E. Gordeliy, E. Detournay, Oribi: implicit fixed grid algorithm to simulate propagation of shallow hydraulic fractures, 2010. Available from: <<http://purl.umn.edu/57327>>.
- [46] R.S. Carbonell, Self-similar solution of a fluid-driven fracture, Ph.D. Thesis, University of Minnesota, Minneapolis, October 1996.
- [47] T. Belytschko, T. Black, Elastic crack growth in finite elements with minimal remeshing, *Int. J. Numer. Methods Eng.* 45 (1999) 601–620.
- [48] N. Moës, J. Dolbow, T. Belytschko, A finite element method for crack growth without remeshing, *Int. J. Numer. Methods Eng.* 46 (1999) 131–150.
- [49] N. Moës, A. Gravouil, T. Belytschko, Non-planar 3d crack growth by the extended finite element and level sets – part i: mechanical model, *Int. J. Numer. Methods Eng.* 53 (2002) 2549–2568.
- [50] J.E. Dolbow, M. Gosz, On the computation of mixed-mode stress intensity factors in functionally graded materials, *Int. J. Solids Struct.* 39 (2002) 2557–2574.
- [51] E. Béchet, H. Minnebo, N. Moës, B. Burgardt, Improved implementation and robustness study of the X-FEM for stress analysis around cracks, *Int. J. Numer. Methods Eng.* 64 (2005) 1033–1056.
- [52] M. Gosz, B. Moran, An interaction energy integral method for computation of mixed-mode stress intensity factors along non-planar crack fronts in three dimensions, *Eng. Fract. Mech.* 69 (2002) 299–319.
- [53] B. Martin-Perez, S.J. Pantazopoulou, M.D.A. Thomas, Numerical solution of mass transport equations in concrete structures, *Comput. Struct.* 79 (2001) 1251–1264.